Observations and scaling of the upper mixed layer in the North Atlantic

I. Lozovatsky,[1,2] M. Figueroa,[3,4] E. Roget,[3] H. J. S. Fernando,[1] and S. Shapovalov[5]

Received 8 September 2004; revised 12 January 2005; accepted 28 February 2005; published 21 May 2005.

[1] The dependence of the mixed layer depth h_D on the sea surface fluxes is analyzed based on measurements taken along a cross-Atlantic section 53°N. A linear function $h_D \approx 0.44L_f$, where $L_f = u_*/f$ is the Ekman scale, well represents the influence of the wind stress u_* and rotation f on the mixed-layer deepening, thus indicating that the influence of convective mixing in late spring at this latitude is of a lesser importance. Also, data showed reasonable correlation of h_D with the stratified Ekman scale $L_{fN} = u_*/\sqrt{fN_{pc}}$, where N_{pc} is the buoyancy frequency in the pycnocline, according to $h_D \approx 1.9L_{fN}$. In both cases the highest correlation between h_D and the corresponding lengthscales is achieved when u_* values taken 12 hours in advance of the mixed layer measurements were used, which may signify the adjustment time of inertial oscillations to produce critical shear at the base of the mixed layer. The vertical profiles of the dissipation rate $\varepsilon(z)$ are parameterized by two formulae that are based on the law of the wall scaling $\varepsilon_s(z) = u_*^3/0.4z$ and the buoyancy flux J_b: $\varepsilon_1(z) = 2.6\varepsilon_s(z) + 0.6J_b$ and $\varepsilon_2(z) = \varepsilon_s(z)$ $\varepsilon_s(z) + 3.7J_b$. The first parameterization is used to calculate the integrated dissipation $\tilde{\varepsilon}_{int}$ over the mixing layer, which was found to be ~3–7% (5% on the average) of the wind work E_{10}. The positive correlation between h_D and $\tilde{\varepsilon}_{int}/E_{10}$ suggests that in deeper quasi-homogeneous layers a larger portion of the wind work is consumed by viscous dissipation vis-à-vis that is used for entrainment. As such, the mixing efficiency, which is based on integral quantities, is expected to decrease with the growth of the mixed layer.

Citation: Lozovatsky, I., M. Figueroa, E. Roget, H. J. S. Fernando, and S. Shapovalov (2005), Observations and scaling of the upper mixed layer in the North Atlantic, *J. Geophys. Res.*, *110*, C05013, doi:10.1029/2004JC002708.

1. Introduction

[2] Direct measurements of small-scale shear in the upper quasi-homogeneous layer (UQHL) of oceans and lakes allow one to assess the kinetic energy dissipation rate ε in the boundary layer and its dependence on atmospheric forcing and background hydrophysical properties. Such measurements are discussed in a large number of publications [e.g., *Dillon et al.*, 1981; *Shay and Gregg*, 1984; *Imberger*, 1985; *Lombardo and Gregg*, 1989; *Moum et al.*, 1989; *Anis and Moum*, 1995; *Brainerd and Gregg*, 1995; *Terray et al.*, 1996; *Smyth et al.*, 1997; *Soloviev et al.*, 2001; *Stips et al.*, 2002]. To analyze the influence of surface fluxes on averaged vertical profiles of ε in the upper ocean, various scalings have been advanced and tested. Most of the microstructure data used for UQHL studies, however, had been collected in equatorial, tropical, and subtropical regions (e.g., PATCHEX and TOGA-COARE). Except for turbulent measurements taken in the Arctic Ocean under the ice cap [*Padman and Dillon*, 1991; *McPhee and Stanton*, 1996] and in Antarctic waters [*McPhee et al.*, 1996], only a few studies exist on the dependence of ε on atmospheric forcing at relatively high latitudes [*Simpson et al.*, 1996; *Lozovatsky et al.*, 1999; *Inall et al.*, 2000; *Burchard et al.*, 2002; *Bolding et al.*, 2002; *Lass et al.*, 2003]. All of these observations, however, have been made in shallow coastal zones (e.g., Black Sea and Malin Shelf) or in shallow seas (North Sea and Baltic Sea). In his comprehensive review on geographic distribution of ocean mixing, *Gregg* [1999] shows the sites of microstructure measurements in the open ocean, and all of them are located south of 40°N. No measurements at higher latitudes have been reported ever since.

[3] Seasonal variations of atmospheric forcing are most distinct in midlatitudes, between 40°N and 60°N in the Northern Hemisphere. During the warm season (late spring to early autumn), atmospheric heat flux is communicated into the ocean through the sea surface, but in the winter and early spring, large areas of the North Atlantic Current are influenced by upward heat flux, which triggers convection.

[1]Environmental Fluid Dynamics Program, Mechanical and Aerospace Engineering, Arizona State University, Tempe, Arizona, USA.
[2]Also at P. P. Shirshov Institute of Oceanology, Russian Academy of Sciences, Moscow, Russia.
[3]University of Girona, Campus de Montilivi, Girona, Spain.
[4]Now at Department of Physical Oceanography, Centro de Investigación Científica y Educación Superior de Ensenada, Ensenada, Baja California, Mexico.
[5]P. P. Shirshov Institute of Oceanology, Russian Academy of Sciences, Moscow, Russia.

0148-0227/05/2004JC002708$09.00

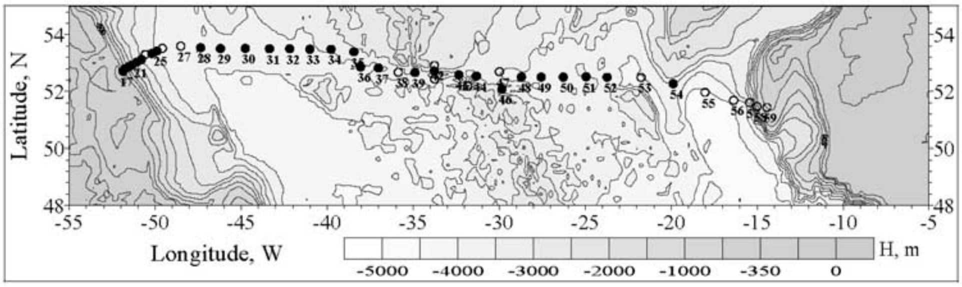

Figure 1. Cross-Atlantic transect taken by R/V *Akademik Ioffe* (18 April to 1 May 2001). Stations with MSS and NBIS measurements are marked by solid circles; those without MSS profiling are shown by open circles. The station numbers must be read as 917–959. The map shows bottom topography in the region.

Prevailing high winds generate and maintain turbulence in the UQHL. The probability of storm events during transition seasons (e.g., winter-spring) in the region is much higher than that at the low latitudes, and these events set up intrinsic spatiotemporal scales of mixing in the upper ocean. The ensuing mixing determines the development and characteristics of UQHL. As such, thermohaline and microstructure measurements in UQHL at a zonal, cross-ocean,

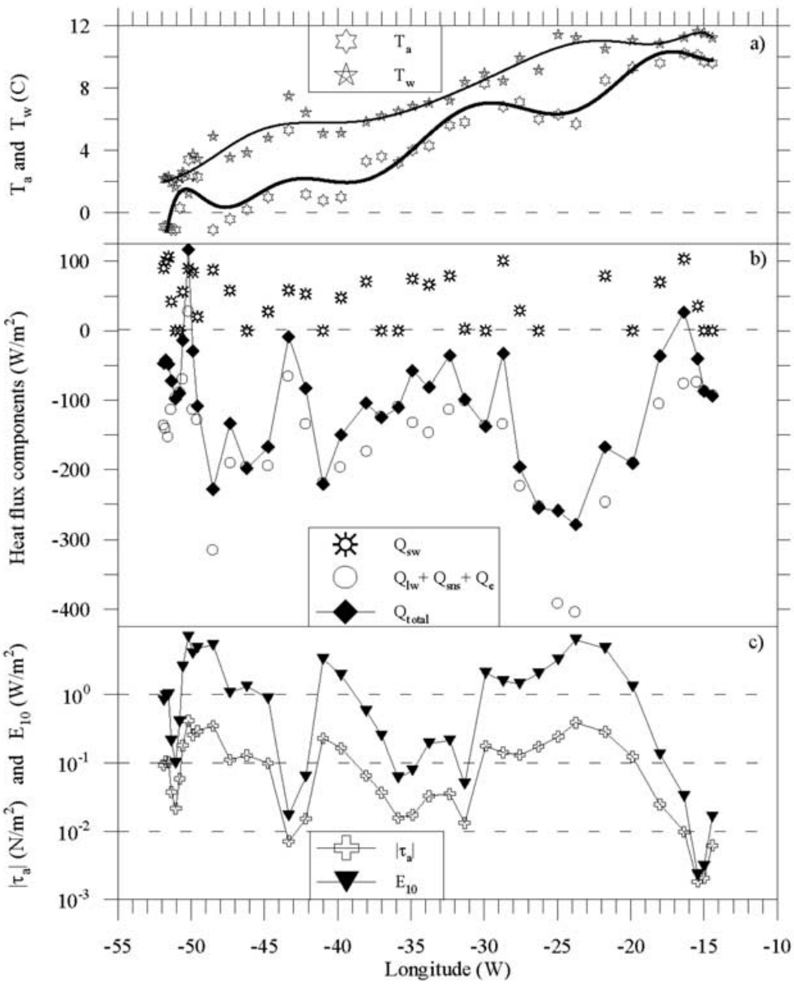

Figure 2. Along-track meteorological data at drift stations: (a) the wind T_a and sea surface T_w temperatures; (b) the components of total Q_{total} heat flux: Q_{sw}, incoming short wave radiation and a sum $Q_{lw} + Q_{sns} + Q_e$ of long-wave radiation Q_{lw}, sensible Q_{sns}, and latent Q_e heat fluxes, respectively; (c) the wind stress $|\tau_a|$ and wind work E_{10} 10 m above the sea surface. The large-scale trends of temperature variations in Figure 2a are obtained by polynomial approximation.

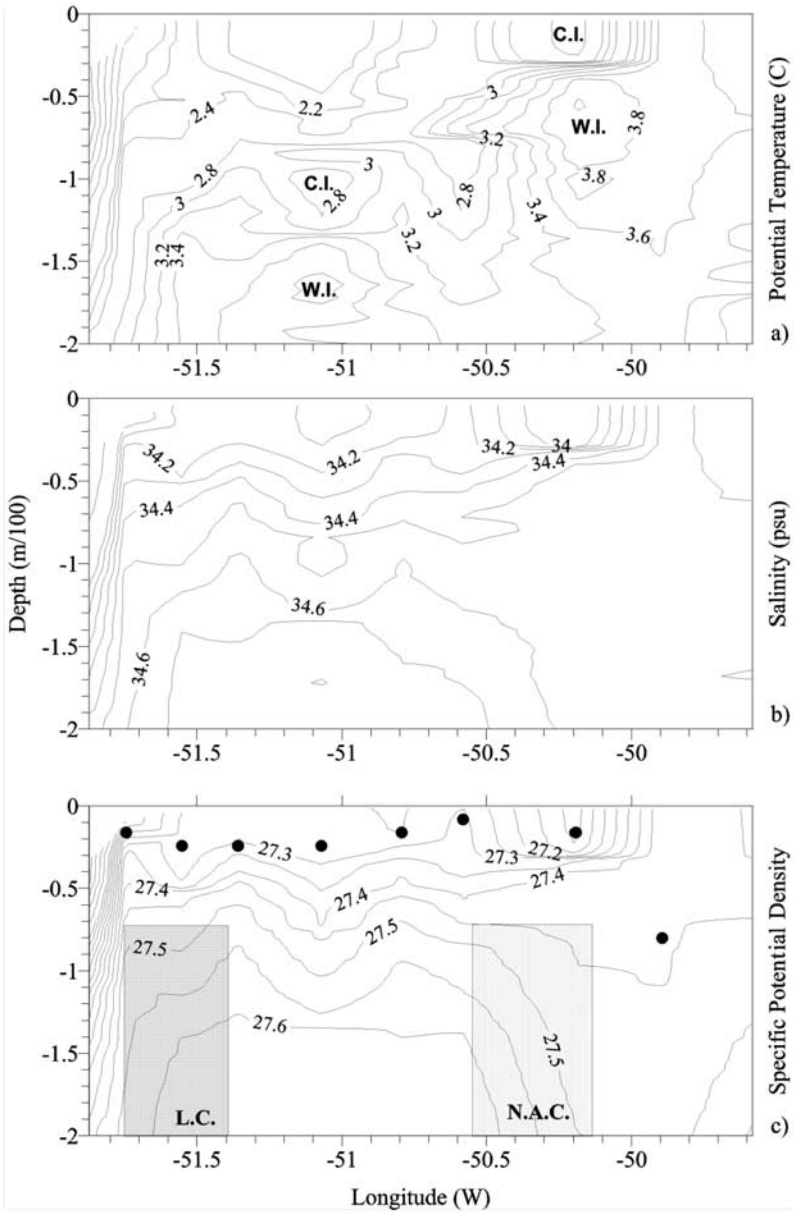

Figure 3. Upper 200-m (a) potential temperature, (b) salinity, and (c) potential density contour plots along the slant section of transect (stations 917–926). Cold (C.I.) and warm (W.I.) intrusions are marked in Figure 3a. Approximate positions of the Labrador Current (L.C.) and a branch of the North Atlantic Current (N.A.C.) are shown in Figure 3c along with the estimates of MLD (dots).

upper-midlatitude transect can give valuable information on basin-scale variability of mixing intensity. In this paper we analyze such measurements taken in the upper 200 m of the Atlantic along 53°N during the ninth cruise of R/V *Akademik Ioffe* in April 2001 (Figure 1).

[4] The observations, instrumentation and data processing are described in section 2 with further details in Appendix A. Because microstructure data so obtained are significantly influenced by both space and time variability of atmospheric and ocean dynamics, they are unsuitable for a complete process-orientated study on UQHL turbulence. Therefore this paper is focused on bulk properties of upper ocean mixing in the winter-spring transition season, which is characterized by predominantly stormy winds and convection-favorable surface buoyancy flux. In section 3, we describe air-sea fluxes, analyze CTD and ADCP contour plots in the upper 200-m layer, and examine ageostrophic currents and the estimates of Ekman transport along the transect. The relationships between the mixed layer depth (MLD) and sea surface fluxes are examined in section 4. The vertical distribution of dissipation in MLD is analyzed in section 5, and attempts are made to parameterize the dissipation rates by using the similarity theory for wind- and convective-induced turbulence. In section 6, the integral of dissipation over the MLD is compared with the wind work at the sea surface, and a discussion is given on the

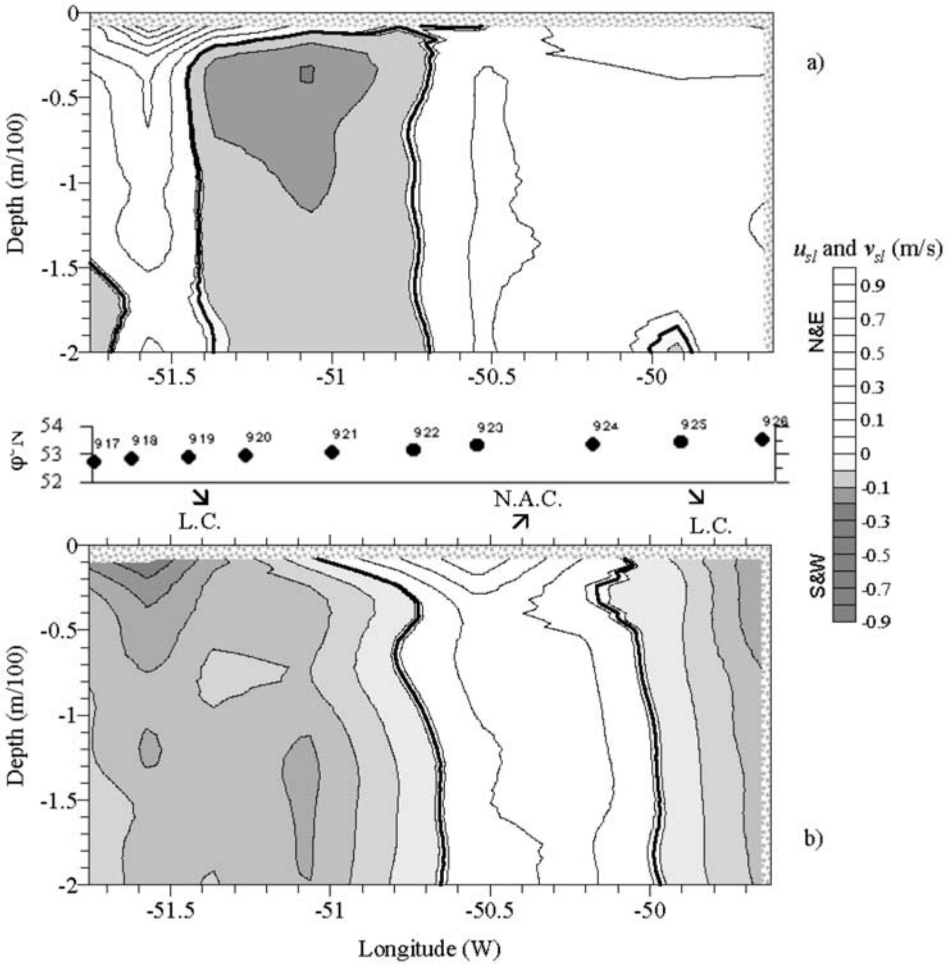

Figure 4. ADCP currents (station data only) in the upper 200-m layer at the Canadian slope section of transect (stations 917–926). (a) Across-slope current component u_{sl} directed roughly southwest-northeast (positive sign). (b) Along-slope (southeast-northwest) current component v_{sl}. The arrows indicate approximate positions of the Labrador Current (L.C.) and a narrow branch of the North Atlantic Current (N.A.C.) at this transect and their general directions.

relationship between the magnitude of dissipation and the layer thickness. The summary is presented in section 7.

2. Observations and Instrumentation

[5] Full-depth CTD profiles and water samples were taken at 42 stations, located along an approximately 53°N transect from the Labrador coast to the shelf of Ireland. Neil Brown Mark III (NBIS) profiler attached with a 12-bottles Rosette water sampler was used. The distance between stations was about 30 miles in the deep sea, and in the coastal zones it was less. Prior to the cruise, all NBIS sensors were calibrated at the testing facility of the Federal Department of Marine Navigation and Hydrography (BSH, Hamburg). The CTD data were processed according to the WOCE standards. The salinity obtained at every station using an Autosal 8400B salinometer was used to control the conductivity channel of NBIS.

[6] A shipboard-mounted ADCP equipped with GPS navigation was employed for measuring the vertical profiles of horizontal velocity components u and v in the depth range 16–600 m with a vertical resolution of 8 m. ADCP data were collected between the stations and during the drifts. Only the drift-station ADCP data were used for further analysis. Standard meteorological parameters were continuously recorded during the cruise by an onboard automatic meteorological station “Wetos 625” and also using a portable automatic “Davis Weather Monitor II”.

[7] The CTD data were mainly intended for studies of interannual and decadal variations of water properties and climate change in the transitional zone between the subtropical and subpolar gyres of the North Atlantic [*Tereshchenkov et al.*, 2002]. The data also contribute to the analysis of seasonal and low frequency variability of thermohaline structure in the region.

[8] In addition, a set of microstructure data was also obtained using MSS profiler [*Prandke and Stips*, 1998; *Prandke et al.*, 2000] (see Appendix A), but the number of casts were limited (usually 2–3, rarely 7–8). The MSS profiling were conducted in parallel with standard CTD measurements. The microstructure measurements in this region of intense meridional heat transport were helpful

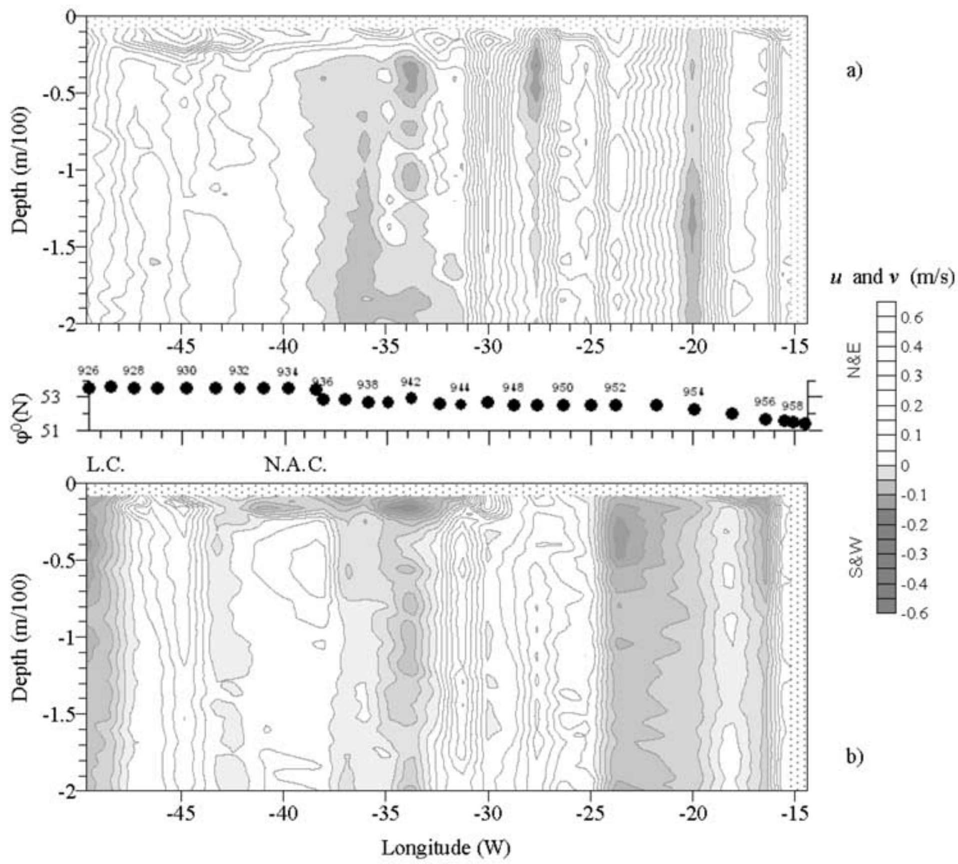

Figure 5. ADCP currents (station data only) in the upper 200-m layer along zonal section of the transect (∼53°N; stations 926–959). (a) Zonal current component u. (b) Meridional current component v. L.C. marks the eastern edge of Labrador Current; N.A.C. is the North Atlantic Current.

for obtaining insights on turbulent mixing in the upper ocean, and to our knowledge, these are the first of their kind in the region.

[9] Stations with MSS and NBIS measurements are shown in Figure 1 by solid circles. The MSS casts have been skipped at a number of stations (open circles) because of severe weather conditions and/or shortage of personnel.

3. Background Hydrographic and Meteorological Conditions

3.1. Meteorological Conditions and Surface Fluxes

[10] Atmospheric forcing at all but two stations was swayed by relatively strong winds and upward heat flux. Time-averaged meteorological data from each station (usually during ∼2.5 hours) were used to calculate the wind stress magnitude $|\tau_a| = (\tau_x^2 + \tau_y^2)^{1/2}$, wind-work at 10 m above the sea surface $E_{10} = W\tau_a^2$ as well as the heat flux components, where W is the wind speed; see Figure 2. These calculations were made using the Matlab Air-Sea toolbox (http://sea-mat.whoi.edu), which employs bulk formulae for air-sea fluxes (with the vertical axis directed downward from the sea surface). Note that Figure 2 is based on meteorological data taken at drift stations only (approximately 6 hours apart on the average), when winds did not exceed 17 m/s. Therefore the averaged "station wind speed" is $\langle W_{st} \rangle$ = 8.7 m/s with rms(W_{st}) = 4.6 m/s. Combining the station measurements with those taken during 12 days of sailing between the stations, the mean wind speed $\langle W \rangle$ was evaluated as 10.7 m/s. Two periods of severe stormy weather, with winds exceeding 12 m/s on 19–20 April (between stations 923 and 926) and on 27–28 April (between stations 952 and 954) were encountered throughout the observations. The maximum winds of $W_{\max}$ = 29 m/s were registered on 28 April. Two other shorter stormy weather events took place between stations 933 and 935, on the night of 22 April ($W_{\max}$ = 26 m/s) and stations 941–942 on 24 April ($W_{\max}$ = 13 m/s). The peak values of $|\tau_a|$ rose to 0.2–0.4 N/m^2, and peak wind work E_{10} achieved 4–6 W/m^2.

[11] The sea surface temperature T_w exceeded the air (wind) temperature T_a (Figure 2) at all stations, which together with high winds ensured the dominance of convection-favorable heat flux along the transect. The mean difference $\langle T_w - T_a \rangle$ = 2.55°C and rms ($T_w - T_a$) = 1.57°C.

3.2. Hydrography of the Transect

[12] The transect roughly coincided with the climatologic position of the annual-mean zero wind stress curl (WSC), which borders subtropical and subpolar gyres of the North Atlantic [*Willebrand*, 1978; *Hellerman and Rosenstein*, 1983; *Ehret and O'Brien*, 1989]. This zone closely correlates with the position of the Gulf Stream and then turns to the east following the North Atlantic Current [*Marshall et*

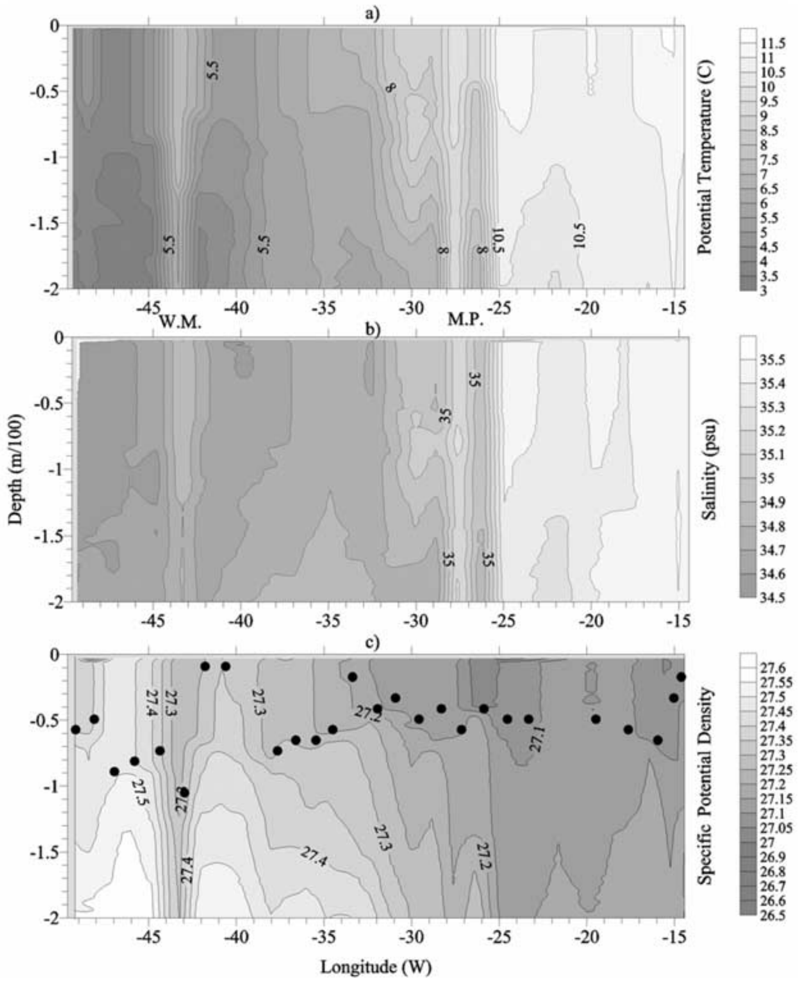

Figure 6. Upper 200-m layer (a) potential temperature, (b) salinity, and (c) potential density contour plots along a zonal trans-Atlantic section (~53°N; stations 926–959, data at the stations only). W.M. marks a warm meander; M.P. indicates a warm-cold meander pair. The MLD estimates are shown in Figure 6c by dots.

al., 2001]. To the north of this line the climatologic WSC is positive, thus forcing a cyclonic subpolar ocean gyre. To the south, an anticyclonic subtropical gyre is present, driven by negative WSC. Deviations from these climatologic states are most frequently observed during the winter-spring and autumn-winter transitional seasons [*Halpern et al.*, 1994]. The maps of WSC patterns for the second part of April 2001 are shown at the IFREMER website (http://www.ifremer.fr/cersat/facilities/browse/mwf/qscat_week.htm) based on weekly averaged CERSAT data. During the first week of our measurements, the WSC mean field was very patchy, indicating high variability of winds. From 23 to 29 April, the averaged WSC shows well-defined anticyclonic WSC over the central and eastern part of the transect with typical values of -2×10^{-7} Pa/m. The basin-scale variations of WSC are likely to be responsible for the observed general west to east deepening of the thermocline (Figure 3).

[13] There are two distinct segments of the cross-basin section, which exhibit different thermohaline structures and flow dynamics in the upper layer. The first one is a slant section of 10 stations between 52.71°N, 51.87°W and 53.52°N, 49.58°W (stations 917–926), which is mainly influenced by cold along-slope Labrador Current. Starting from station 926 (Figure 1), approximately zonal section containing 32 deep-ocean NBIS stations (between 53.6°N, 48.51°W and 51.43°N, 14.43°W) was taken, crossing multiple branches and meanders of the North Atlantic Current.

[14] A general increase with depth of potential temperature (θ), salinity (S), and specific potential density (σ_θ) in the upper 200 m of the across-slope section is shown in Figure 3. The contribution of stable salinity gradients to the density stratification prevails over nonstable temperature gradients, ensuring stable vertical structure of mean density. Mesoscale thermohaline isopycnal intrusions, which are seen in Figures 3a and 3b, do not substantially affect the density spatial structure. The only near-surface lens of cooler and fresher water, centered at the latitude 50.2°W, clearly exhibits local baroclinic fronts, which may be associated with a mesoscale eddy or about ~20 miles diameter meander. The depth of upper quasi-homogeneous layer west of 50°W does not exceed 22 m. At station 925 (53.43°N, 49.9°W), the thickness of UQHL sharply increases to 80 m due to preceding wind-induced stormy mixing.

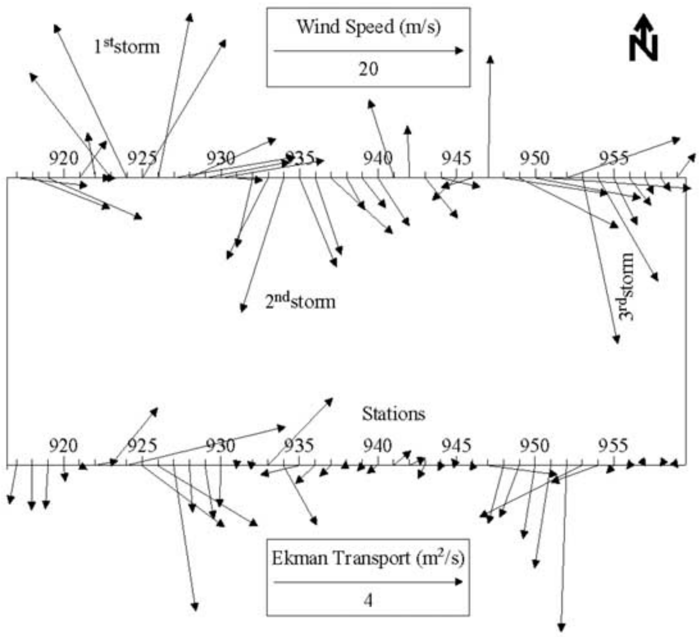

Figure 7. Wind vectors $\vec{W}_{st}$ averaged over the working time at each drift station (top axis) and corresponding estimates of the Ekman transport (bottom axis) at hydrographic stations along the transect. The right-directed $\vec{W}_{st}$ arrows represent westerly winds.

[15] In the thermohalocline, below 50 m, a dome of isopycnal contours (Figure 3c) can be related to quasi-geostrophic countercurrents that are associated with a large cyclonic eddy (or a meander). These local baroclinic fronts may also represent a branch of the Labrador Current (the southeast upslope flow west of 51.4°W) and oppositely directed branch of the North Atlantic Current (offshore northwestern flow between 50.5° and 50.2°W). These currents are well identified at the along-slope section of ADCP velocity shown in Figure 4b. A boundary between the two is evident at 50.65°W. A map of the geostrophic circulation in the Labrador Sea [*Lazier and Wright*, 1993, Figure 2] shows a narrow northwestern flow penetrating into the mainstream of the Labrador Current at 53°N, 50.5°W, just in the middle of our transect, and then turning to the north and east. Therefore we interpret the observed northern current centered at about 50.3°W as a branch of the warmer North Atlantic Current rather than a section of an eddy or meander of the Labrador Current. This is corroborated by the ADCP data in Figures 4a and 4b, where a southeastern flow is seen east of 50°W, west of which the flow is northward. The Labrador Current extends farther to the east up to 48°W (see the southeastern flow at the left side of ADCP panels, Figure 4); then the transect meets the North Atlantic Current (Figure 5). The corresponding contour plots of θ, S, and σ_θ in the upper 200 m along the zonal section (stations 926–959) are given in Figure 6. The temperature and salinity continuously increase eastward and the density decrease as the transect crosses the Gulf Stream transformed waters. There are, however, two distinct regions at 44°–45°W and between 25° and 28°W with highly alternating horizontal gradients of θ, S, and σ_θ. The first is associated with a warm meander, where θ at z = 150 m equals to 6.6°C (station 931), while θ = 3.4°C 30 miles to the west (station 930) and θ = 4.1°C 30 miles to the east (station 932). The ADCP meridional component (Figure 5b) clearly depicts two counterflows of anticyclonic circulation in this meander. In the second region, a loop of warm-cold meander pair leads to the formation of local frontal zones between stations 948 and 951. The temperature difference at z = 200 m across the eastern front (warm meander) exceeds 2.5°C, and across the western front (cold meander) it is about 3.5°C. The internal frontal zone, which separates cores of two meanders, is characterized by $\delta\theta > 2.5$°C at a distance of 40 miles. The basin-scale and large-to-mesoscale variability of thermohaline and density structure in the upper 200-m layer below is mainly governed by geostrophic circulation. Time-space variations of atmospheric forcing determine ageostrophic dynamics of the upper layer and synoptic scales variability of MLD.

3.3. Ageostrophic Currents and Ekman Transport

[16] *Chereskin and Roemmich* [1991] (hereinafter referred to as CR91) and *Wijffels et al.* [1994] (hereinafter referred to as WFB94) were among the first to analyze ageostrophic dynamics of the upper oceanic layer using ADCP and CTD measurements in equatorial and tropical regions. Ageostrophic meridional transport across 11°N in the Atlantic Ocean was calculated in CR91 and similar investigation for 10°N in the Pacific was made in WFB94. At these latitudes, the interannual variability of wind speed is relatively small.

[17] At 53°N, a series of atmospheric cyclones that often crosses the Atlantic in early spring significantly influences

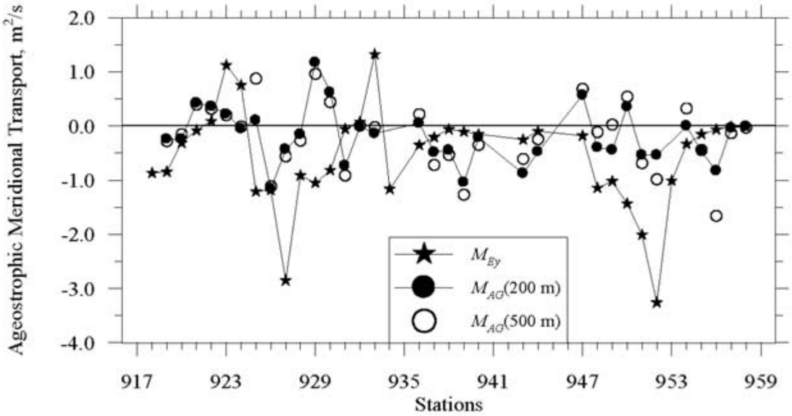

Figure 8. Wind stress-based Ekman transport M_{Ey} (1) and MLD ageostrophic transports M_{AG}(200 m) and M_{AG}(500 m) obtained from ADCP and NB measurements with reference level of zero ageostrophic velocity at z = 200 and 500 m, respectively.

the upper layer. The Ekman transport vectors (Figure 7) point to the prevalence of southward and eastward ageostrophic flows in the upper layer during stormy periods. (Note that the Ekman transport is directed 90° to the right of the wind vectors shown in Figure 7, top.) The transport amplitudes M_E,

$$M_E = \frac{|\tau_a|}{f\rho_w},$$

have been calculated using the wind stress $|\tau_a|$, the sea surface density ρ_w and the Coriolis parameter f. The averaged amplitude $\langle M_E \rangle$ is about 1 m^2/s; the highest M_E = 3.4–3.5 m^2/s are found at stations 927 and 952.

[18] Following CR91, we first computed geostrophic currents between stations, interpolated the results to the station locations, and then subtracted the geostrophic velocity from averaged ADCP meridional component, assuming that flow maintains a geostrophic balance at a specific depth z_G below MLD. This depth was assigned by CR91 as z_G = 250 m; WFB94 choose z_G = 125 m. We computed ageostrophic velocities V_{AG} using two reference levels, z_G = 200 and 500 m. The results did not show any statistically significant difference, suggesting that the ageostrophic meridional transport across 53°N in the Atlantic is mainly limited to depths below upper 200-m layer. If, within the upper layer, V_{AG} represents a wind-driven current component, then the meridional Ekman transport M_{AG} at each station can be obtained by integrating V_{AG} over the thickness of this layer. Because current measurements obtained by ship-mounted ADCP are noisy in the upper 15–20 m layer [*Pollard and Read*, 1989], we extrapolated V_{AG} from z_{cw} = 16 m to the sea surface assuming it to be a constant $V_{AG}(z) = V_{AG}(z_{cw})$ in the near-surface layer following recommendations of WFB94. The estimates of M_{AG}(200), M_{AG}(500), and the meridional component of wind stress-based transport M_{Ey} are given in Figure 8. At high winds, $|M_{Ey}|$ exceeds $|M_{AG}|$, which can be accounted for the uncertainty in extrapolation of ADCP data into the upper 16-m layer. Although a slab-like current structure is often assumed in upper mixed layer models [*Price et al.*, 1986], there is a possibility that current amplitudes may increase significantly toward the sea surface, thus requiring more accurate extrapolation scheme of $V_{AG}(z)$ than used here. Note CR91, for example, achieved a reasonable correspondence between M_{AG} and M_{Ey} using a linear increase of V_{AG} above z = 20 m.

[19] Although M_{AG} along the 53°N transect is usually smaller than M_{Ey} (the mean $\langle M_{AG}\ (200)\rangle = -0.18$ m^2/s and $\langle M_{Ey}\rangle = -0.55$ m^2/s), the directions of M_{AG} and M_{Ey} are generally consistent for transport amplitudes greater than ±0.3 m^2/s; only at stations 929 and 930, a significant difference was observed. In the later case, the southward Ekman transport M_{Ey}, supposedly driven by strong westerly winds, was found to be opposite to the northward ageostrophic transport $M_{AG} \approx 1$ m^2/s. This disparity could attribute to one or more of the following: (1) the incorrect extrapolation of V_{AG} between 0 and 16 m, (2) the ageostrophic flow is not wind driven, and (3) the penetration depth of the drift current exceeds 200 m, which is, however, unlikely. At station 930, a shallow drift current with distinct southward meridional component is able to impede the northward ageostrophic transport, but at station 929 the meridional component is positive everywhere while decreasing with depth. Therefore a significant influence of non-wind-driven ageostrophic component is possible here, and the locally observed winds may not be representative of regional-scale drift currents.

[20] We also analyzed the current reversal depth (CRD), which is the shallowest depth (below z = 16 m) where ADCP current vector changes its direction of rotation. Two examples of ADCP current spirals showing clockwise and counterclockwise rotation of ADCP vector with depth in the upper layer are given in Figure 9. Clockwise rotation was observed in 19 out of 34 averaged ADCP profiles. The velocity amplitude, however, did not always decrease with depth as it is supposed to be in the Ekman boundary layer, which is bounded by the geostrophic flow beneath. The rest of the profiles with counterclockwise rotation are not consistent with the Ekman drift. Because the ADCP data return a combination of dynamical components (wind-induced, geostrophic, buoyancy-forced, inertial oscillations, etc.), the Ekman spiral could have been overshadowed by a more powerful process. It is also possible that at the time of

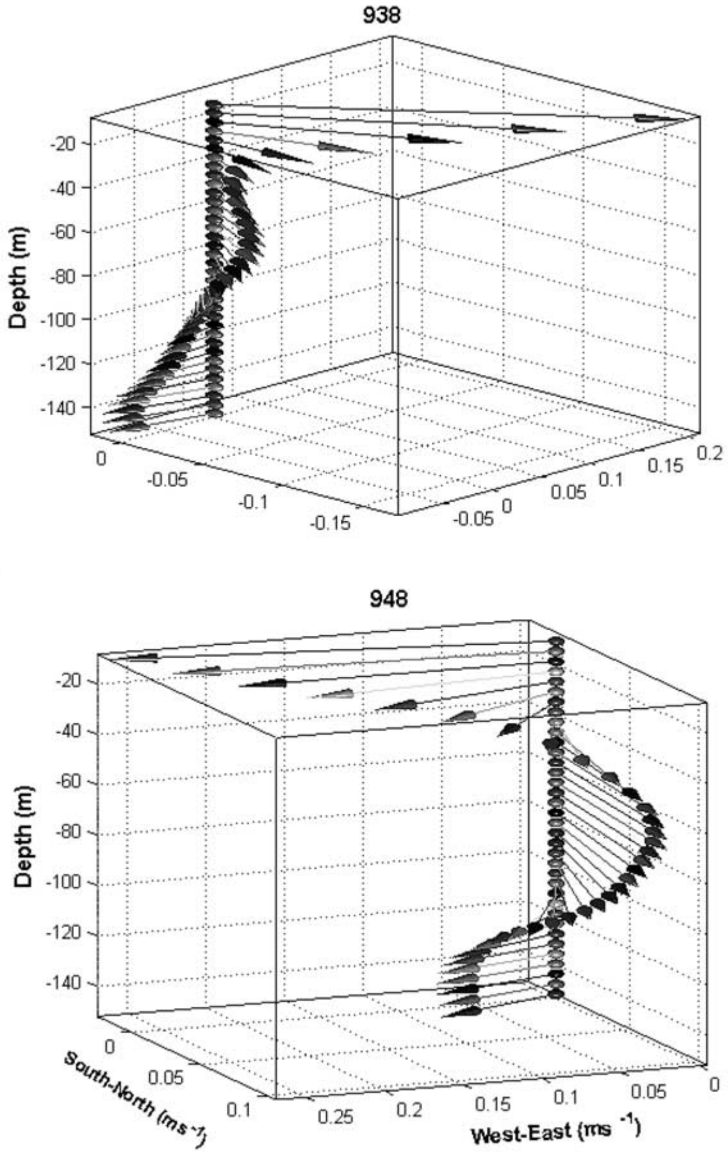

Figure 9. Examples of ADCP vector spirals showing (top, station 938) clockwise (upper panel, St. 938) and (bottom, station 948) counterclockwise rotation in the upper layer. The spirals were plotted using the interpolated $u(z)$ and $v(z)$ profiles (Δz_{int} = 2 m) while the original ADCP data were sampled at Δz = 8 m.

measurements, the drift currents at a number of stations were far from stationary state required for a well-defined Ekman spiral.

4. Mixed-Layer Depth

[21] The along-transect variation of the mixed layer depth MLD is shown in Figure 10, calculated using the approach given in Appendix B. Free-falling, 1-m averaged MSS profiles usually exhibit slightly deeper MLD (h_{MSS}) compared to the MLD obtained from 2-m interpolated and prefiltered NB-CTD profiles (h_{NB}). The mean $\langle h_{NB} \rangle$ = 44.5 m, the median of h_{NB} is 48 m, and rms (h_{NB}) = 25.2 m. Because MSS measurements have not been carried out at all stations, we will mainly refer to h_{NB} (h_D hereinafter) as the characteristic MLD. The observed mixed layer depth varies in the range of 6–110 m, the deepest h_D being at station 931.

[22] If we compare MLD statistics with those of CRD (the current reversal depth), it appears that $\langle$CRD$\rangle$ = 46.9 m and med (CRD) = 48 m are almost the same as the mean and the median of MLD given above. This may indicate that the mixed layer depth coincides, on the average, with the depth penetrated by the drift currents. The correspondence becomes clearer if we compare the mean difference between CRD and MLD separately for clockwise and counterclockwise profiles using 2-m interpolated ADCP data. For the first group (19 stations), the mean difference $\langle$CRD − MLD$\rangle$ is only 2 m, while for the second group the mean difference is 7.2 m. We may conclude that the mesoscale spatiotemporal variations of MLD and CRD along the

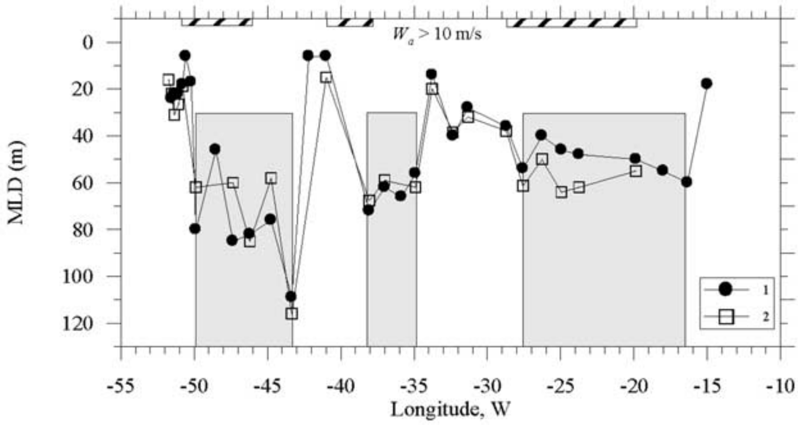

Figure 10. Mixed layer depth (MLD) obtained from NB-CTD (line 1) and MSS (line 2) density profiles. Three periods with winds exceeding 10 m/s are marked along the upper axis. The sections with increase of MLD (shaded areas) exhibit a space-time shift (delay) in relation to the segments of stormy winds. The time shift, up to 1 hour, between NB and MSS casts in part is attributed to the observed differences between lines 1 and 2 at several stations.

transect are broadly consistent. Also note that because of the time shift between NB and ADCP profiles, the differences between observables at individual stations could be due to internal wave displacements and horizontal inhomogeneities.

[23] Three shaded segments in Figure 10, with noticeable increase of MLD ($h_D > 50$ m), are associated with periods of high winds ($W > 10$ m/s; see the hatched segments along the upper axis in Figure 10), which precede somewhat the periods of enhanced mixed-layer deepening. The magnitude of the heat flux also increases with higher winds (Figure 2), ensuring a larger buoyancy flux J_b.

[24] To quantify the relationship between atmospheric forcing and MLD, we calculated the normalized cross-correlations functions R_{hu_*} (Δt) and R_{hJ_b} (Δt), where Δt is the corresponding time lag. To make these calculations possible, we produced the equally spaced time records of MLD and fluxes by the linear interpolation of measurements at each station. The time step Δt_{int} = 6 hours was chosen for the interpolated records, because approximately 12 days of observations provided 49 interpolation points, while the measurements were taken at 42 time locations (stations). Arranging the data as time series, not as space variables, for the correlation analysis is based on the assumption that the main cause of the mixed layer deepening and restratification is associated with synoptic scale variations of u_* and J_b driven by storm events. Horizontal scales of the regions where MLD exceeds 50 m are 250–350 km, consistent with the scales of atmospheric cyclones at these latitudes.

[25] The correlation between h_D and friction velocity u_* exhibits (Figure 11) a statistically confident maximum R_{hu_*} (Δt) = 0.71 at the time shift Δt = 12 hours. The highest correlation R_{hJ_b} (Δt) between h_D and J_b, however, is only 0.4 at Δt = 0, and it is lower elsewhere. Because the 95% confidence level for nonzero correlation is 0.34, R_{hJ_b} (Δt) is insignificant at all Δt. This indicates that the deepening of mixed layer during our measurements was governed by wind stress, the influence of buoyancy flux being of lesser importance. This can be verified by comparing MLD with the Monin-Obukhov [*Monin and Obukhov*, 1954] scale $L_{MO} = u_*^3/\kappa J_b$, where κ = 0.4 is the von Karman constant.

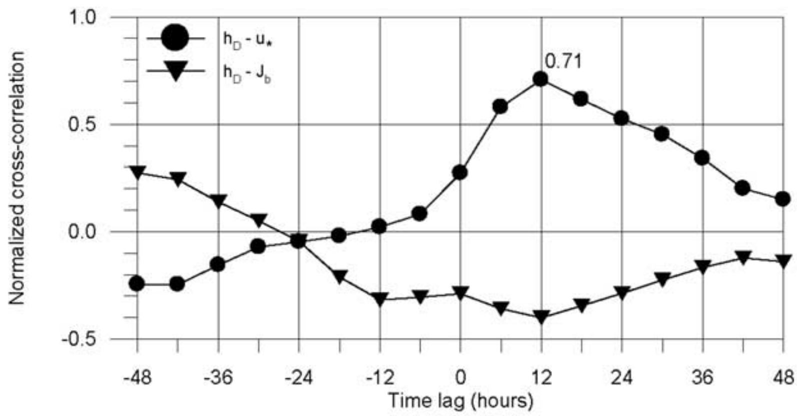

Figure 11. Normalized cross-correlation functions between the mixed-layer depth h_D and friction velocity u_* (dots), and between h_D and the buoyancy flux J_b (triangles).

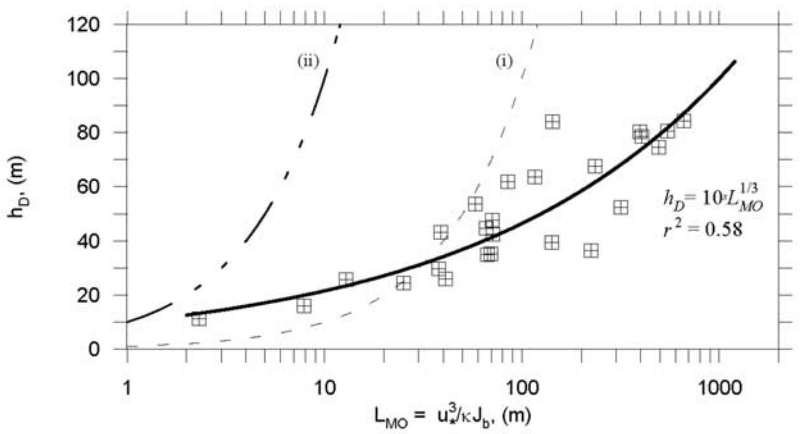

Figure 12. Regressions between the mixed layer depth h_D and Monin-Obukhov scale L_{MO} at stations 926–954, with the friction velocity u_* shifted in time by 12 hours. The buoyancy flux J_b calculated at the time of MLD measurements is shown. The power trend of h_D growth with the increase of L_{MO} is obtained by least squares fitting. Line i corresponds to $h_D/L_{MO} = 1$; line ii gives $h_D/L_{MO} = 10$.

[26] The dependence between MLD and L_{MO} is shown in Figure 12, with the time record of u_* shifted ahead by Δt = 12 hours. At stations 926–954, the buoyancy flux was always convection favorable; therefore L_{MO} is positive everywhere. The power approximation in Figure 12, $h_D \sim L_{MO}^{1/3}$, indicates a linear dependence between the MLD and friction velocity. The dependence on the buoyancy flux J_b is weak. Following *Lombardo and Gregg* [1989] (hereinafter referred to as LG89), we show two lines in Figure 12: $h_D/L_{MO} = 1$ and $h_D/L_{MO} = 10$, which bound the range of h_D when the wind stress and buoyancy flux play comparable role in the development of mixed layer. For $h_D/L_{MO} > 10$ (to the left from the "ii" line), convection is a dominant force, but for $h_D/L_{MO} < 1$ (to the right from the "i" line), the wind stress is a prevailing factor. Figure 12 shows that only at three stations (where h_D less than 35 m) the contributions of both wind stress and buoyancy flux in shaping the mixed layer depth are comparable. The vast majority of points lie below the $h_D/L_{MO} = 1$ line indicating that in the spring season, convection is less important in maintaining the mixed layer depth compared to wind-induced mixing.

[27] Given the linear dependence of h_D on u_*, it is possible to surmise that the Ekman lengthscale $L_f = u_*/f$ is a better candidate to scale MLD than L_{MO}. Because the average response of MLD is lagged the change of friction velocity by about 12 hours, we plotted the regression of h_D on L_f, shifting the records by Δt = 12 hours. As evident from Figure 13a, the dependence between L_f and shifted in time (space) MLD can be reasonably approximated by a linear function $h_D \approx 0.44 L_f$ with the coefficient of determination $r^2 = 0.92$. This correlation does not hold when the time shift is not used, as evident from Figure 13b. It is possible that the observed time lag is associated with the spin-up time of inertial oscillations, which enhance shear and thus vertical mixing at the base of the mixed layer [see, e.g., *Pollard et al.*, 1973]. A similar result has been reported by *Lentz* [1992] for coastal upwelling waters, with the time shift ranging from (5–6) to (10–12) hours. The result shown in Figure 13 suggests that winds associated with spring storms in the North Atlantic have to work for about 12 hours in order to effectively erode the existing stratification, entrain water from the underlying pycnocline, and develop a UQHL with the mean thickness of ~45 m. Much shorter time is needed, however, for the upper layer turbulence to respond to rapidly increasing winds [see, e.g., *Anis and Moum*, 1995]. Also, turbulence decays quickly when atmospheric boundary forcing is ceased. The above interpretation assumes that the measurements of MLD represent a quasi-

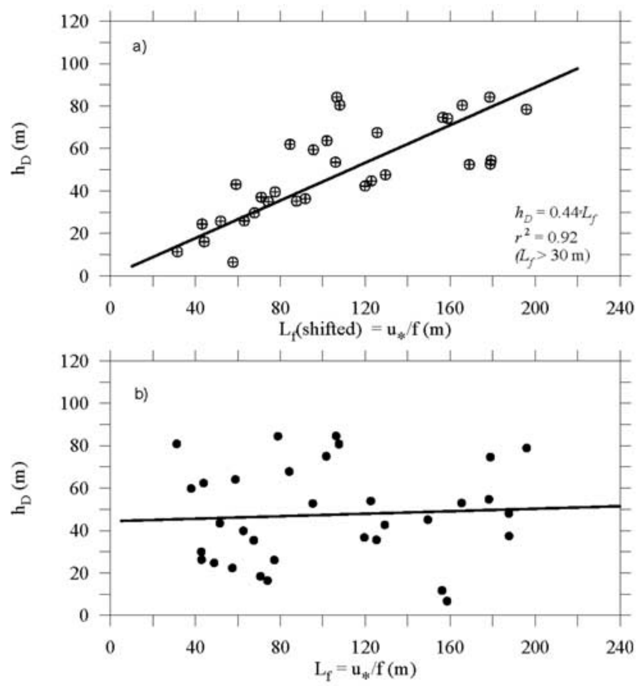

Figure 13. (a) Regressions between the mixed layer depth h_D and 12-hour forward shifted Ekman scale L_f. (b) The same variables without time shift. A linear growth of h_D with L_f (for $L_f > 30$ m), which is seen in Figure 13a, vanishes in Figure 13b.

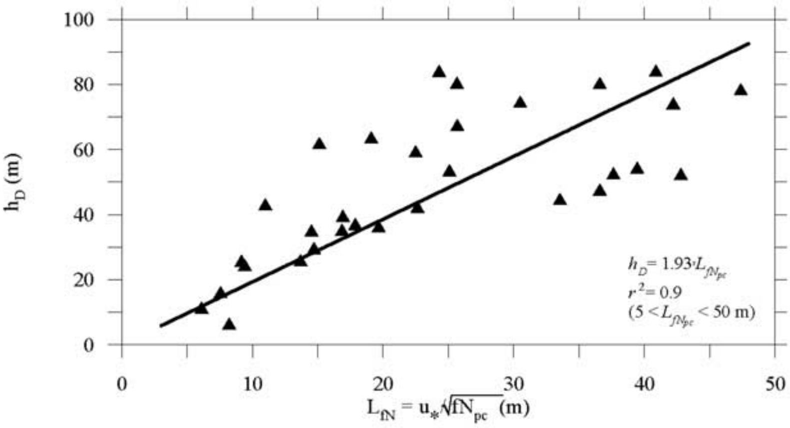

Figure 14. Scaling of mixed layer depth h_D by using the stratified Ekman lengthscale $L_{fN} = u_*/\sqrt{fN_{pc}}$. The estimates of friction velocity u_* are shifted ahead in time by 12 hours in L_{fN} calculation.

stationary state of the mixed layer. At some stations, especially those taken in the beginning of stormy events, it is definitely not true. This may be one of the reasons why data in Figure 13 exhibit relatively wide scatter around linear trend.

[28] The mixed layer results can also be interpreted on the premise that upon introduction of a wind stress the UQHL deepens until MLD reaches $L_{fN} = u_*/\sqrt{fN_{pc}}$, where N_{pc} is the buoyancy frequency at the upper boundary of the pycnocline (obtained by a linear fit to the density profiles over the first 10–15 m below UQHL). As pointed out by *Pollard et al.* [1973], the subsequent growth is slow. Therefore L_{fN} can be a good indicator of MLD after a storm. Scaling of MLD by L_{fN} [*Pollard et al.*, 1973] has been explored by *Weatherly and Martin* [1978] and *Lentz* [1992] for the bottom boundary layer and by *Zilitinkevich and Esau* [2002] for the atmospheric boundary layer. Figure 14 shows a plot of h_D versus L_{fN} with u_* shifted ahead in calculating L_{fN}. The goodness of linear fit in Figure 14 ($r^2 = 0.9$) is slightly lower than in Figure 13a, but this difference is statistically insignificant. A relatively wider scatter in Figure 14 may indicate that N_{pc} is either calculated with a higher uncertainty (because of highly nonlinear density profile in the pycnocline) or it does not significantly influence the MLD at later stages of the mixed-layer deepening. The regression in Figure 14 shows that on the average, the ratio $h_D/L_{fN} \approx 1.9$. *Pollard et al.* [1973] reported $h_D/L_{fN} = 1.7$, and *Weatherly and Martin* [1978] found $h_D/L_{fN} = 1.3$. Various one-dimensional models of thermocline formation [e.g., *Niiler and Kraus*, 1977; *Price et al.*, 1986; *Lozovatsky et al.*, 1998] suggest that the ratio h_D/L_{fN} tends to reach 1.7 at large times of numerical calculations. As such, we can surmise that at most stations the observed mixed layers were at a slow phase of growth, close to an equilibrium state.

5. Vertical Structure of the Dissipation Rate

[29] A composite plot of individual 1-m averaged ε samples taken from the mixed layer at all stations is given in Figure 15, where the depth-sorted, bin-median estimates of the dissipation (large symbols; 100 samples in each bin; the total number of samples is 2487) are shown. Two regimes can be identified: a sharp decrease of the bin-median dissipation $\hat{\varepsilon}(z)$ with depth at $z < z_{cw}$, where $z_{cw} = 16$ m, and much slower decline of $\hat{\varepsilon}(z)$ in the depth range $h_D > z > z_{cw}$. The least squared approximations, which were

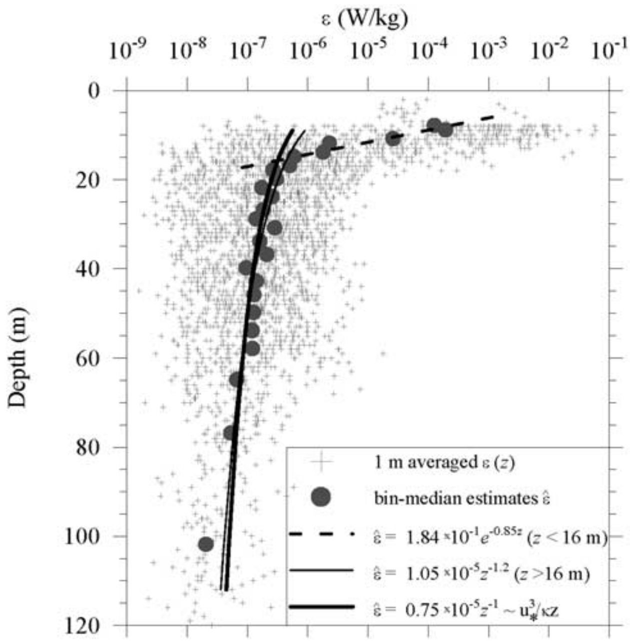

Figure 15. Kinetic energy dissipation rate in the upper turbulent layer at all stations of measurements (2487 samples). The depth-sorted, bin-median estimates of the dissipation (100 samples in each bin) $\hat{\varepsilon}$ are shown by large symbols. The best least squares approximations (exponential, dashed line; power, thin solid line) are given for two sections of $\hat{\varepsilon}(z)$ profile, 2 m < z < 16 m and 16 m < z < h_D, respectively. The transition depth $z_{cw} = 16$ m was selected by careful inspection of data and considering the calculation of two empirical fits.

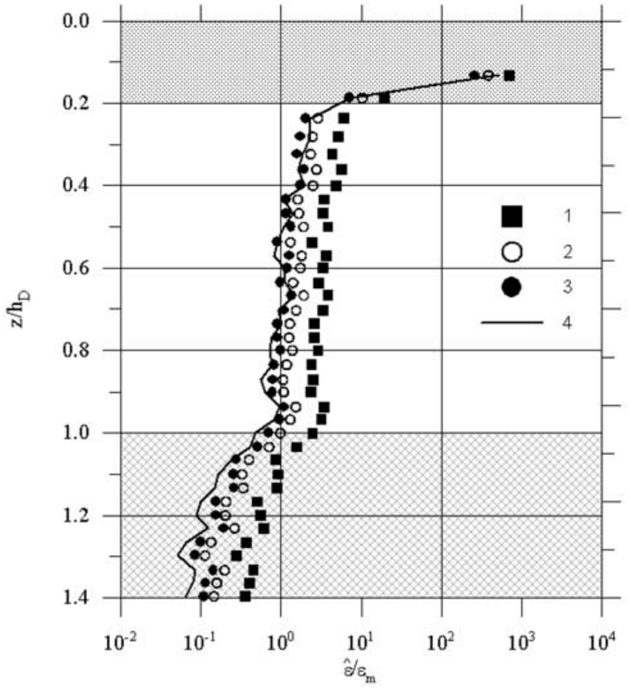

Figure 16. Bin-median profiles of the dissipation rate in the upper turbulent (mixing) layer $\hat{\varepsilon}$ normalized by the modeling dissipation ε_m. Here, "1" is the law of the wall given by equation (1); "2" is equation (2) [LG89]; "3" is a modified formulae of LG89, equation (3), and "4" is ε_n based on the logarithmic-linear similarity model of the velocity profile, leading to equation (4) with c_{bm} = 3.7.

separately applied to these two sections, give the following equations:

$$\hat{\varepsilon}(z) = 1.84 \times 10^{-1} e^{-0.85z} \quad \text{for } z < 16 \text{ m}$$

$$\hat{\varepsilon}(z) = 1.05 \times 10^{-5} z^{-1.2} \quad \text{for } z > 16 \text{ m},$$

respectively. Turbulence in the near-surface layer, $z < z_{cw}$, is significantly affected by surface waves and the observed exponential decrease of $\hat{\varepsilon}$ with depth generally supports the wave-induced scaling for dissipation proposed by *Anis and Moum* [1995]. However, because we used a falling, not a rising, profiler ε measurements in the near-surface layer could have been contaminated by the unsteady falling speed, occasional cable tension, and ship rolling. Therefore this study excludes the depth range $z < z_{cw}$. Formal power law fitting given above for $z > z_{cw}$ can also be satisfactory represented by an inverse power function $\hat{\varepsilon}$ (z) = 0.75 × 10^{-5} z^{-1}, in the spirit of the well-known "law of the wall,"

$$\varepsilon_s(z) = \frac{\tilde{u}_*^3}{\kappa} z^{-1}, \tag{1}$$

which has been used in several studies to represent the dissipation profile in the surface layer [i.e., *Dillon et al.*, 1981; *Soloviev et al.*, 1988]. Despite the bin-median estimates of $\hat{\varepsilon}$ (z) in Figure 15 roughly follow equation (1), it should be noted that the law of the wall can only be used as a zero order model for $\hat{\varepsilon}$ (z), given the influence of the surface buoyancy flux. Analyzing microstructure measurements taken in the upper layer of Eastern Subtropical Pacific, LG89 scaled the dissipation profiles in the range $1 < h_D/L_{MO} < 10$ as

$$\varepsilon(z) = c_s \varepsilon_s(z) + c_b J_b, \tag{2}$$

where ε_s (z) is the dissipation induced by the surface stress (equation (1)) and c_s = 1.76, c_b = 0.58 are empirical constants. *Stips et al.* [2002] examined equation (2) in the context of convective mixing in Lake Maggiore, Italy, and found noticeable departure of the measured $\varepsilon(z)$ from the LG89 scaling. *Smyth et al.* [1997] fitted the dissipation profiles measured in the upper layer of equatorial Pacific under light winds, several hours after the passage of a squall, with c_b = 0.6 (the value of c_s was not specified in that paper).

[30] In Figure 16, we show four normalized profiles of the dissipation rate $\varepsilon_n(z_n)$ based on the bin-median estimates of the depth-sorted ε population (the population includes all individual samples at all stations). The data collected at all stations were sorted over the normalized depth $z_n = z/h_D$ and the bin-median estimates of z_n, and ε_n were calculated over 100 consecutive samples in each bin. Here $\varepsilon_n = \hat{\varepsilon}/\varepsilon_m$ and the modeling function $\varepsilon_m(z_n)$ is given by equation (1) for profile 1 and by equation (2) for profile 2. It is clear that (1) reasonably represents the dissipation of vertical structure in the depth range $\sim 0.4 < z_n < 1$, but the absolute value of normalized dissipation is overestimated approximately 3 times ($\langle \varepsilon_n \rangle$ = 3.01 ± 0.52) because the normalized median-bin dissipation is expected to be constant, $\varepsilon_n(z_n) = 1$, for $0 < z_n < h_D$, if u_* is the only governing parameter of its vertical structure. In the surface layer ($0 < z_n < 0.2$), ε_n sharply departs from the approximately constant level due to measurement errors and direct wave forcing. The parameterization of LG89 (equation (2)) does shift ε_n closer to 1, yielding $\langle \varepsilon_n \rangle$ = 1.46 ± 0.27 in the depth range $z_n \approx 0.4-1.0$ (profile 2 in Figure 16). This shows that a combination of ε_s and J_b given by equation (2) is helpful, but some modification of the empirical coefficients is needed to achieve a better scaling.

[31] As has been shown in Figure 12, our data set does not contain measurements during the periods where convective mixing substantially prevailed over the wind-induced turbulence in UBL (the condition $h_D/L_{MO} > 10$ of LG89 is never satisfied; if L_{MO} is calculated based on in situ unshifted u_*, the situation does not change). As such, it is not possible to obtain confident estimates of c_b as in the case of almost pure convective balance, $\varepsilon \approx c_b J_b$, considered by LG89. Therefore, in order to find a semi-empirical modeling profile of $\varepsilon_m(z)$ that gives the best fit to our data, we employed two approaches that are based on the similarity theory. First, note that the pioneering *Monin and Obukhov* [1954] paper proposes c_b = 0.6, and ensuing measurements give c_b = 0.58 and 0.72 for oceans and c_b = 0.64 for the atmospheric boundary layers. *Imberger* [1985] and *Imberger and Ivey* [1991] suggest c_b = 0.46. In this paper, we take the original value c_b = 0.6, so that any observations

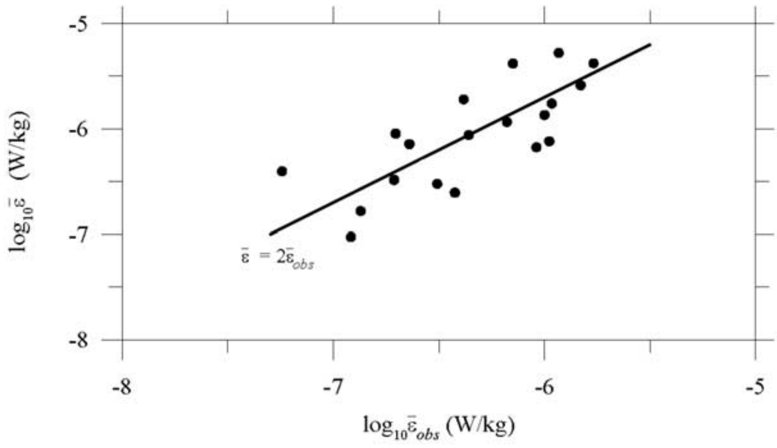

Figure 17. Correlation between the measured $\bar{\varepsilon}_{obs}$ and "modeled" $\bar{\varepsilon}$ (through equation (3)) integrated dissipation estimates per unit depth.

of the dissipation rate over $0.6J_b$ should be attributed to the wind-induced shear production $c_s\varepsilon_s$ (thus defining c_s). The best fit for the data gives

$$\varepsilon_{m1}(z) = 2.6\varepsilon_s(z) + 0.6J_b, \tag{3}$$

which is shown in Figure 16 by profile 3. This gives very close proximity, on the average, to $\varepsilon_n = 1$, yielding $\langle\varepsilon_n\rangle = 1.05 \pm 0.25$ in the depth range $0.4 < z/h_D < 1$. Note that for $0.4 > z/h_D > 0.2$, ε_n remains almost constant $\hat{\varepsilon}/\varepsilon_{m1} = 2.3 \pm 0.24$ and only then the normalized dissipation rapidly increases toward the sea surface.

[32] Winds, during the measurements reported by LG89, were distinctly lower (E_{10} = 0.2–0.6 W/m^2) than those observed at 53°N, where the median E_{10} = 1 W/m^2, and E_{10} exceeded 0.6 W/m^2 for 60% of the data. The buoyancy flux, however, was approximately the same in both experiments, about 3×10^{-8} W/kg on the average. This difference in wind work may possibly account for the larger value of c_s = 2.6 (compared to c_s = 1.76 of LG89) proposed by our work.

[33] If high (and possibly low) winds lead to the variation of c_s in equation (2)/equation (3), the application of $c_s \leq 1.8$ could be limited to a specific range of relatively moderate winds, while a larger constant (c_s = 2.6 in our case) is more appropriate for high winds. This is not an unusual situation; bulk formulae, for example, employ different values of the friction coefficient when calculating the wind stress for low and high winds. Despite this uncertainty, it is quite surprising that a simple similarity approach can be used to describe the basic shape of the dissipation profile in the upper oceanic layer, which is influenced by numerous complex processes such as Langmuir vortices, inertial waves, and others.

[34] Alternatively, if all excessive dissipation above ε_s calculated by equation (1) is included in c_bJ_b with an empirical constant $c_b \equiv c_{bm}$, then the best fit for $\varepsilon_n = \hat{\varepsilon}/\varepsilon_{m2}$ is given in Figure 16 by profile 4 using c_s = 1 and

$$\varepsilon_{m2}(z) = \varepsilon_s(z) + c_{bm}J_b, \tag{4}$$

with c_{bm} = 3.7. The proximity of line 4 to ε_n = 1 is good: $\langle\varepsilon_n\rangle = 0.98 \pm 0.34$ for z/D = 0.4–1.0. It is interesting that the empirical constant c_{bm} falls in the range of values that are often used for stratified atmospheric surface layer with log linear velocity profile [*Bussinger et al.*, 1971; *Dyer*, 1974; *Stull*, 1988]. Equation (4) can also be interpreted as the result of interaction between shear and convective instabilities, with latter producing "extra" mixing. In engineering and meteorology, the combined influence of shear and convection is called forced convection. Application of equations (3) and (4) for scaling of dissipation in the regions with substantially different hydro-meteorological conditions than considered here should be done with caution, given the possible differences in the structure of turbulence and dynamical processes.

6. Column-Integrated Dissipation

[35] Because turbulence in the mixed layer was dominated by the wind stress, we attempted to estimate the fraction of wind work E_{10}, which dissipates in the upper turbulent layer, using equation (3) and calculating the column-integrated dissipation rate as

$$\tilde{\varepsilon}_{\rm int} = \int_0^{h_\varepsilon} \rho_w\varepsilon(z)dz, \tag{5}$$

where h_ε is the mixing layer depth, which in our case at almost all stations is equal to MLD. *Oakey and Elliot* [1982] were among the first to make estimates of the dissipation of the wind work E_{10} in the upper turbulent layer using direct measurements of small-scale shear by an airfoil sensor. They reported $\tilde{\varepsilon}_{int} \approx 0.01E_{10}$ for a 20-m near-surface boundary layer.

[36] Because it is not possible to retrieve microstructure measurements from the upper near-surface layer ($z < z_{cw}$), we used the "model" dissipation profiles (equations (3) and (5)) to calculate $\tilde{\varepsilon}_{int}$ in the mixing layer ($0 < z < h_\varepsilon$) with local values of u_*, J_b, and h_ε at each station. The integrated "measured" dissipation $\tilde{\varepsilon}_{obs}$ at every station was also obtained for the inner turbulent layer of thickness $h_{obs} = h_\varepsilon - z_{cw}$. The estimates of mean dissipations $\bar{\varepsilon} = \tilde{\varepsilon}_{int}/h_\varepsilon$ and

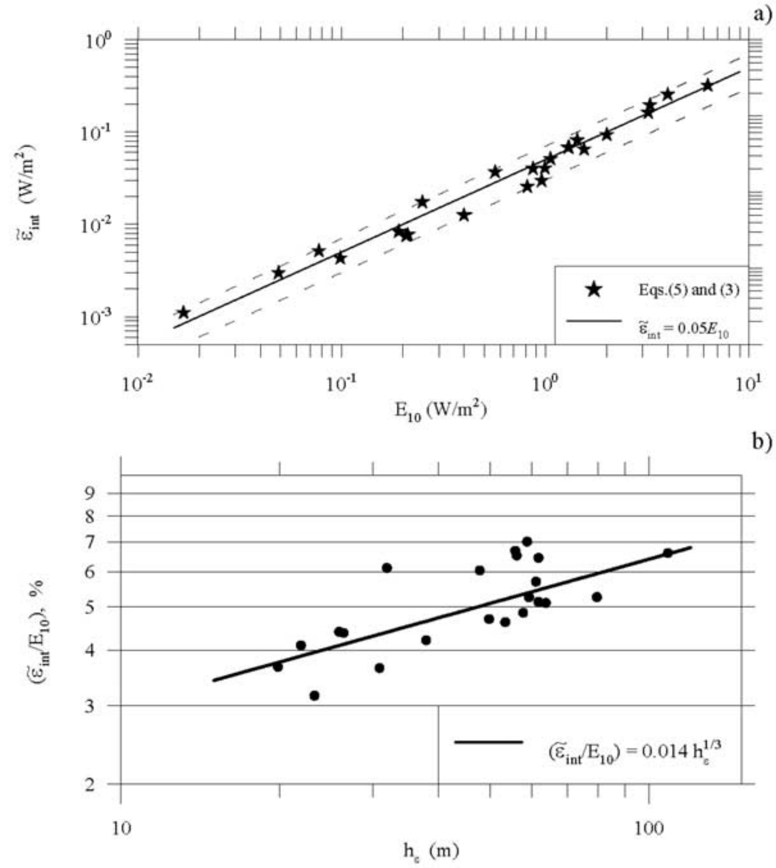

Figure 18. (a) Integrated dissipation in the upper mixing layer as a function of the wind work E_{10}. The calculation of $\tilde{\varepsilon}_{int}$ is based on equations (5) and (3) using local values of u_*, J_b, and h_ε at each station. The dashed lines show the lower, $\tilde{\varepsilon}_{int} = 0.03E_{10}$, and the upper, $\tilde{\varepsilon}_{int} = 0.07E_{10}$, limits for the linear regression. (b) Dependence between the thickness of the mixing layer and the ratio $\tilde{\varepsilon}_{int}/E_{10}$. The correlations are based on 22 stations with distinct mixing layers.

$\bar{\varepsilon}_{obs} = \tilde{\varepsilon}_{obs}/h_{obs}$ given in Figure 17 demonstrate a good correlation, showing that $\bar{\varepsilon}$ is about twice $\bar{\varepsilon}_{obs}$.

[37] A plot of $\tilde{\varepsilon}_{int}$ (E_{10}) in Figure 18a indicates that the data samples can be well approximated by $\tilde{\varepsilon}_{int} = 0.05E_{10}$. This suggests that on the average, $\tilde{\varepsilon}_{int}$ may account for about 5% of the wind work at 10 m above the sea surface; the ratio $\tilde{\varepsilon}_{int}/E_{10}$ varies between 3 and 7%. This is consistent with the estimates of *Richman and Garrett* [1977] that the rate of energy entering the ocean from the wind is in the range 2–10% of the wind work E_{10}. It is likely, however, that larger MLDs are associated with higher mean dissipation rates, when turbulence is active within the upper boundary layer and vice versa. Some of the outstanding questions in this context are: Is the fraction of wind work that dissipates during the mixing layer formation independent on the layer depth? Does turbulence in deeper layers consume a larger fraction of wind work than that in shallower layers? The answer is given in Figure 18b, where a clear tendency of $\tilde{\varepsilon}_{int}/E_{10}$ growth is associated with larger h_ε. The approximated empirical power law function is simply given to emphasize the trend.

[38] The observed growth of the ratio $\tilde{\varepsilon}_{int}/E_{10}$ with increase of h_ε seems to be consistent with results of numerical and laboratory experiments [*Kantha and Clayson*, 2000a, 2000b] which suggest that in growing turbulent layers, entrainment rate decreases in time. In other words, as the mixed layer deepens, the entrainment rate decreases owing to the increase of the Richardson number or to the inability of eddies to raise dense fluid against the negative buoyancy of thermocline. In order to accommodate this dynamical constraint and realize the bulk energy balance, the column-averaged dissipation rate increases in the mixed layer, as evident from the laboratory mixed-layer measurements of *Kit et al.* [1997]. The increase of $\tilde{\varepsilon}_{int}/E_{10}$ ratio may also indicate a change of integrated mixing efficiency $\tilde{\gamma}$ with respect to E_{10} with the increase of MLD (this is unrelated to the mixing efficiency and flux Richardson number based on local variables). One of the customary assumptions that the averaged buoyancy flux due to entrainment is proportional to the energy imparted by the wind, therefore, should be revisited in view of the above finding that this proportionality constant can be variable.

7. Summary

[39] The response of the mixed layer depth (MLD) to short-term (synoptic) variations of atmospheric forcing in the North Atlantic was analyzed using profiling measure-

ments taken at 42 stations along 53°N in April 2001. The microstructure data obtained concurrent with CTD measurements allowed estimation of kinetic energy dissipation rate in the upper turbulent layer at high-midlatitudes and parameterization of its vertical structure using momentum and buoyancy fluxes at the sea surface. Atmospheric forcing during 12 days of observations was characterized by relatively high winds (the mean wind speed is 10.7 m/s) and convection-favorable surface heat balance. The sea surface temperature was on the average 2.5°C higher than the air temperature. The transect, which followed the climatologic position of zero annually averaged wind stress curl (WSC), crossed the Labrador Current and multiple branches and meanders of the North Atlantic Current. The basin-scale variation of WSC is likely responsible for the observed general deepening of the thermocline from the west to the east. Mesoscale thermohaline frontal intrusions were mainly observed in the pycnocline not affecting the vertical structure of density in the upper mixed layer. Three strong storms were encountered during the measurements, and the wind stress at drift stations reached 0.2–0.4 N/m^2.

[40] The averaged amplitude of Ekman transport $\langle M_E \rangle$ calculated using the wind stress is about 1 m^2/s, but during the storms, the magnitude of M_E goes up to 3.4–3.5 m^2/s. The ageostrophic flows in the upper layer were mainly southward and eastward. The meridional ageostrophic transports M_{Ey}, were usually larger than that calculated using the residuals between ADCP and geostrophic velocities, M_{AG}, but it was in the same direction as M_{Ey} when $|M_{AG}|$ exceeds 0.3 m^2/s.

[41] To identify the MLD at each station, an algorithm developed by *Kara et al.* [2000] was employed. The results were carefully checked manually, and corrections were introduced, if needed; less than 10% of MLD estimates were so corrected. The deepest observed mixed layer depth h_D was 110 m, the mean was $\langle h_D \rangle$ = 45 m, the median of h_D is 48 m and rms(h_D) = 25.2 m. The MLD was compared with the current reversal depth (CRD is specified as the shallowest depth where current vector changes the sign of its rotation). The mean and median estimates for CRD appeared to be very close to those for MLD (47.9 and 48 m, respectively) suggesting that the drift currents were mostly confined to the upper mixed layer.

[42] The highest correlation (0.71) between the MLD and friction velocity u_* was found when u_* data were time advanced by 12 hours. The correlation of MLD with the surface buoyancy flux J_b was weak. The ratio between h_D and the Monin-Obukhov lengthscale $L_{MO} = u_*^3/J_b$ based on the time shifted u_* indicates that almost at all stations $h_D/L_{MO} < 1$, suggesting the dominance of wind-induced mixing over convection. Parameterization of MLD in terms of the Ekman scale $L_f = u_*/f$ (with time-shifted u_*) yielded the following linear dependence:

$$h_D \approx 0.44 L_f \qquad L_f > 30 \text{ m},$$

with the coefficient of determination, r^2 = 0.92. As pointed out by a referee, it is worth noting that the proportionality constant above 0.44 is approximately equal to the canonical value of von Karman's constant κ = 0.41, emphasizing small influence of buoyancy on mixed-layer turbulence.

[43] The analysis suggests that a 45-m-deep mixed layer is associated with a mean friction velocity of $\langle u_* \rangle = 1.2 \times 10^{-2}$ m/s working approximately for 12 hours. Because our sampling rate was made equal to 6 hours, the 12-hour time shift should be treated as a rough estimate, but it is close to the typical 8–10 hours delay between u_* and MLD variations reported by *Lentz* [1992]. This time lag can be associated with the spin-up time for the inertial oscillations triggered by storms. On the other hand, the generation of turbulence in the upper layer by rapidly increasing winds is a fast process, as well as the decay of turbulence when the winds cease [*Anis and Moum*, 1995]. Therefore, while the in situ surface fluxes are most appropriate for parameterizing vertical profiles of the dissipation rate, the mixed layer deepening should account for the slow response of thermocline mixing.

[44] The MLD was also correlated with the "stratified Ekman scale" $L_{fN} = u_*/\sqrt{fN_{pc}}$, where N_{pc} is the buoyancy frequency in the pycnocline, assuming that the growth of MLD is arrested by buoyancy when MLD reaches L_{fN}. Using L_{fN} with time shifted u_*, a linear regression of the form

$$h_D \approx 1.9 L_{fN}$$

was obtained with reasonable statistical confidence. This suggests that L_{fN} can be a good indicator for storm-induced MLD. Given that numerical calculations show that in the steady state MLD is about $1.7L_{fN}$, the above result suggests that the mixed layer at most stations may have achieved or close to achieving an equilibrium state.

[45] The vertical structure of the dissipation rate $\varepsilon(z)$ in the depth range $\sim 0.4 < z/h_D < 1$ could not be reasonably represented by the scaling of *Lombardo and Gregg* [1989], but the best possible fit to the data could be reached by a parameterization of the form

$$\varepsilon_{m1}(z) = 2.6\varepsilon_s(z) + 0.6J_b,$$

where $\varepsilon_s(z) = u_*^3/\kappa z$ is the law of the wall. Alternatively, a good correspondence with data could be also obtained using

$$\varepsilon_{m2}(z) = \varepsilon_s(z) + 3.7J_b.$$

The latter assumes that all "excessive" dissipation above ε_s is due to buoyancy production of forced convection. The factor 3.7 before J_b is surprisingly close to that often used for stratified atmospheric surface layer with log linear velocity profile. Despite the fact that turbulent mixing in the upper layer is influenced by numerous complex dynamical processes such as Langmuir circulation and wave breaking, it appears that simple parameterizations based on similarity approaches with some modification can be used to describe essential features of the dissipation profile in the upper oceanic layer.

[46] The column-integrated dissipation rate $\tilde{\varepsilon}_{int}$ over the MLD may account, on the average, for about 5% of the wind work at 10 m above the sea surface E_{10} (however, the ratio $\tilde{\varepsilon}_{int}/E_{10}$ varies between approximately 3 and 7%). The ratio $\tilde{\varepsilon}_{int}/E_{10}$ shows a positive correlation with MLD, indicating the increased column averaged dissipation at

higher MLD. This calls for rethinking of the commonly used modeling assumption of the proportionality between the buoyancy flux due to entrainment and the rate of wind work imparted on the surface.

Appendix A: Measurements of the Dissipation Rate

A1. MSS Profiler

[47] A commercial MSS (Micro Structure System) profiler developed by a consortium of companies, which were participants of the MITPC project (Improved Microstructure Technologies for Marine Near Surface Flux Studies), funded by the European Community [*Prandke et al.*, 2000], was used in this study. The profiler consists of a stainless steel cylinder, 100 cm in length and 10.6 cm in diameter. It encapsulates electronics and a set of sensors at the lower end, protected by a guard. The data are transferred to an on-board computer via an almost neutral buoyancy elastic cable. The same cable is used to recover the profiler after each free-falling cast. To maintain a constant falling speed of about 0.7 m/s, the profiler should have a negative buoyancy of about 1 kg, which can be regulated by special buoyancy rings of different weight. The profiler carries microstructure sensors (for small-scale shear and fast temperature), sensors of conductivity, temperature, and pressure, and a three-component accelerometer. The sensitivity of the microthermistor is 0.001°C, and its response time is 7 ms. The precise temperature sensor (Pt-10) has a sensitivity of 0.001°C, accuracy 0.01°C, and time response 160 ms. The corresponding characteristics of the seven-pole conductivity cell are 0.001 mS/cm, 0.01 mS/cm, and 100 ms, respectively. The vertical resolution of an airfoil shear probe (PNS 98) is limited to 2 cm, determined by the sensor geometry. The laboratory calibration tests of the shear probe indicate a lowest measurable dissipation rates of about 10^{-11} W/kg, although the lowest in situ noise level of shear measurements is equivalent to $\sim 10^{-9}$ W/kg.

A2. Editing and Despiking the Raw Data

[48] Microstructure data are usually noisy, especially at the very first few meters below the surface. Therein, the signals are contaminated by ship-induced movements and transients of the profiler. The data at the end-point of the cast are also heavily contaminated, because of the cable tension, which causes high-amplitude vibrations. Since end segments cannot be recovered by any denoising procedure, they were removed from the analysis. It is not possible to completely eliminate spikes and faulty data segments in microstructure records because of numerous debris, and abrupt failures in communication links or malfunctions of the sensors [*Moum and Lueck*, 1985], and these spikes and contaminated data segments must be identified and removed. Editing microstructure data cannot be done manually, considering the huge amount of information collected by microstructure sensors, and therefore various statistical approaches must be applied. For example, *Prandke et al.* [2000] suggest excluding bad samples or assigning value to them by calculating the mean μ and standard deviation σ for each consecutive pre-determined segment and then marking and replacing the data outside the interval ($\mu \pm n\sigma$), where $n = 2.7$. This type of despiking works well if the data limits are known a priori, or noise is generated by a known source, but this is usually not the case for microstructure measurements. We have developed an interactive, efficient graphic MATLAB interface to identify isolated spikes, bad values, or gaps in the records. Upon completing this step, a procedure similar to that of *Prandke et al.* [2000] was applied, but instead of replacing bad samples by the mean value calculated at each segment, we used a cubic spline interpolation, if the number of bad or missing points was less than 50 (about 5 cm of the record) and set $n = 2$. If a data gap was larger than 5 cm, the record was divided into several separate segments, with none of the gaps exceeding 5 cm.

[49] Sometimes, a localized, narrow-frequency noise can appear in the signal because of the mechanical resonance of the profiler. Such localized peaks, around 40 Hz in our case, were deleted by a Lanczos window [*Hamming*, 1983] designed for a specific wave number band. A band-pass Lanczos filter has a very sharp frequency response function and, therefore, high-amplitude peaks could be removed without significant changes in the adjacent frequency bands.

A3. Influence of Falling Velocity on Small-Scale Shear Profiles

[50] Accurate calculation of the falling velocity w_p of the profiler is an important step in data processing because the output signal of the airfoil sensor e_{out} is proportional to w_p^2, i.e., $e_{out} = \rho S_0 \, w_p^2 \, (du'/dt)$, where S_0 is the cross-sectional area of the cylindrical part of the sensor [*Paka et al.*, 1999]. The time derivatives du'/dz were calculated by computing finite differences, with further filtering by the Butterworth low-pass filter; here the frequency response function is equivalent to a three-point running-averaged filter. To convert the time-sampled signals to the depth-dependent variables, we calculated the falling velocity from a pressure signal, which can be contaminated by wave-induced variations of the sea-surface and possible tilting of the profiler. To reduce the fluctuations in the pressure signal, which in principal ought to be a monotonic function of time, we approximated consecutive segments (usually 25 dbar in length) of data by a second-order polynomial function and then connected the consecutive segments using five-point running averaging filter. The falling velocity, computed as the time derivative of the smoothed pressure signal, minimizes errors in the calculation of du'/dz and hence ε.

A4. Calculation of the Dissipation Rate

[51] After applying all necessary corrections to small-scale shear signal, the dissipation rate ε was evaluated by fitting one-dimensional wave number shear spectra calculated at each 1-m vertical segment to the Panchev-Kesich [*Panchev and Kesich*, 1969] theoretical spectrum

$$E_n(k) = \left(k^{1/3} + \sqrt{\frac{3}{2}}k^1\right) \exp\left(-\frac{3}{2}k^{4/3} - \sqrt{\frac{3}{2}}k^2\right), \qquad \text{(A1)}$$

following recommendations of *Gregg et al.* [1996]. Here the nondimensional wave number $k = \alpha^{3/4}\,\kappa\eta$ is normalized by the Kolmogorov's scale $\eta = (\nu^3/\varepsilon)^{1/4}$, $E_n = E/[\alpha^{9/4}\,(\varepsilon\nu^5)^{1/4}]$ is the dimensionalized spectrum, $\alpha = 0.5$ is the Kolmogorov's constant in the inertial subrange, and κ and $E(\kappa)$ are the

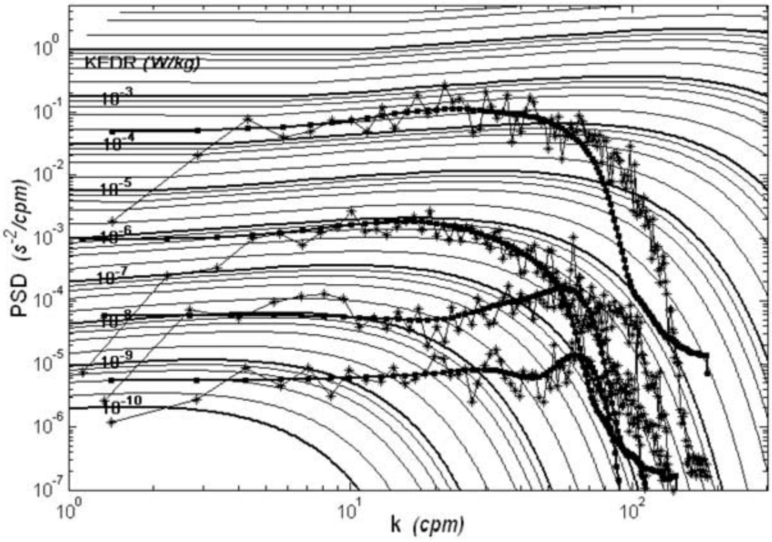

Figure A1. Examples of microstructure shear spectra before (star lines) and after (squared lines) denoising. The theoretical Panchev-Kesich spectra (equation (A1)) are shown by plain continuous lines marked by every next decade of the corresponding ε values.

corresponding dimensional variables (κ is in rad/m). The best fit was usually applied at low and intermediate wave numbers, where signal is less contaminated than at high κ, and the universality of (A1) is assumed. The procedure is shown in Figure A1, where several shear spectra from the mixed layer and thermocline are plotted in the background of theoretical spectra (equation (A1)) for a wide range of ε values. Experimental spectra (star lines) were smoothed (dotted lines) before fitting, and then the corresponding dissipation rates were evaluated. The lowest-level spectrum in Figure A1 represents the noise-level segments of the dissipation measurements, which is about 10^{-9} W/kg.

[52] In Figure A2, we compare the nondimensional Panchev-Kesich [*Panchev and Kesich*, 1969] spectrum and another widely used *Nasmyth* [1970] spectrum, both of which are used as spectral benchmarks. The empirical spectra shown in Figure A2 were taken from several microstructure patches with different mean dissipation rate, which varies over 2 decades of magnitude (from 3.4×10^{-9} to 2.6×10^{-7} W/kg). The integrated dissipations $\tilde{\varepsilon}$ were used for normalization. The experimental spectra show good agreement with the universal spectra at intermediate wave numbers, covering the most important range that embraces the maximum of the dissipation spectrum. The variance estimates obtained by integration of respective normalized spectra differ in magnitude by less than 10%. Note that the Panchev-Kesich spectrum contains more power at lower wave numbers and rolls off slightly faster

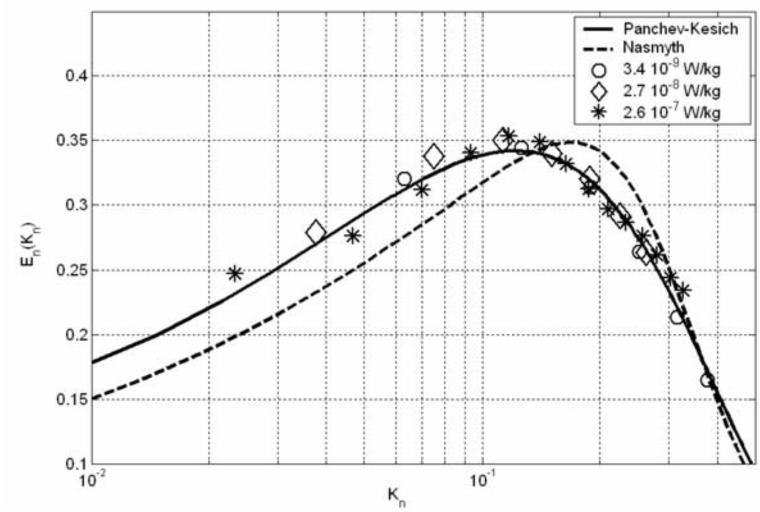

Figure A2. The nondimensional *Nasmyth* [1970] and Panchev-Kesich [*Panchev and Kesich*, 1969] benchmark spectra overlaying the empirical spectra for a range of dissipation rates and the Kolmogorov's constant $\alpha = 0.5$.

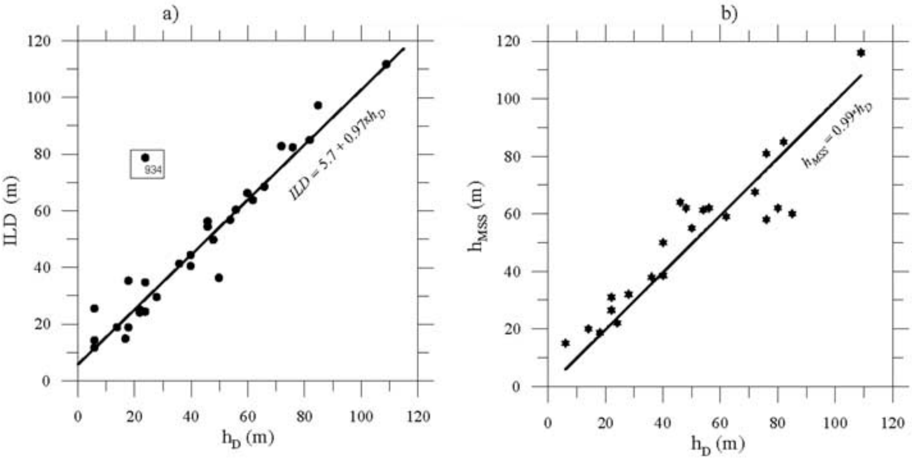

Figure B1. (a) Correspondence between the depth of isothermal upper layer (ILD) and the mixed layer depth h_D. The ILD was calculated using *Kara et al.* [2000] algorithm with $\Delta z = 2$ m and $\delta T = 0.25°C$. The h_D was determined by the difference criteria $\delta\sigma_\theta = 0.02\ \sigma_\theta$ and making a manual correction if necessary. The regression coefficient of determination $r^2 = 0.95$ without taking into account station 934. (b) MLD estimates obtained from NB (h_D) and MSS (h_{MSS}) profiles at the stations where both instruments worked in parallel.

at high wave numbers compared to the Nasmyth spectrum. This difference may affect measurements with high level of dissipation, when small-scale shear at low wave numbers is not well resolved, and therefore a correction is needed when calculating the shear variance. As seen, the MSS data more closely follow the Panchev-Kesich spectrum for the chosen dissipation rates. The best possible adjustment to the Nasmyth spectrum to fit our data gives slightly different estimates for the dissipation rate.

Appendix B: Calculation of the Mixed Layer Depth

[53] The depth of upper quasi-homogeneous layer (UQHL) h_D can be identified as the "isothermal layer depth" (ILD) where the absolute difference between the temperature $T(h_D)$ and that near the sea surface T_w exceeds a prescribed limit δT [*Kara et al.*, 2000]. If the absolute density difference in UQHL $\delta\sigma_\theta = |\sigma_\theta(z_D) - \sigma_{\theta w}|$ is less than a specific $\delta\sigma_\theta$, then h_D is associated with the mixed layer depth MLD [*Brainerd and Gregg*, 1995]. Calculating ILD, *Thompson* [1976] and *Martin* [1985] employed relatively small $\delta T = 0.2°C$ and $0.1°C$, respectively, and a larger $\delta T = 0.5°C$ have been used by *Price et al.* [1986], *Kelly and Qiu* [1995], *Obata et al.* [1996], and *Monterey and Levitus* [1997]. *Lamb* [1984], *Wagner* [1996], and *Qu* [2003] increased δT up to 1°C. The most common values of the density difference $\delta\sigma_\theta$, when calculating the MLD, are in the range $(0.10–0.13)\sigma_\theta$ [*Miller*, 1976; *Levitus*, 1982; *Lewis et al.*, 1990; *Spall*, 1991; *Huang and Russell*, 1994]. A narrower limit, $\delta\sigma_\theta = (0.01–0.03)\sigma_\theta$, was, however, used by *Peters et al.* [1989], *Schneider and Muller* [1990], and *Padman and Dillon* [1991].

[54] Alternatively, ILD and MLD can be identified as layers where vertical gradients of temperature or specific density are smaller than a prescribed value of $\delta T/\delta z$ or $\delta\sigma_\theta/\delta z$, assuming a sharp transition between UQHL and underlying thermohalocline [*Bathen*, 1972; *Lukas and Lindstrom*, 1991; *Richards et al.*, 1995; *Brainerd and Gregg*, 1995]. The threshold gradients are usually set up in the range 0.02–0.05 C/m for $\delta T/\delta z$ and 0.01 kg/m^4 for $\delta\sigma_\theta/\delta z$. An attempt [*Korchashkin*, 1976] has been made to identify layers with constant vertical gradients (including quasi-homogeneous layers) by using difference criteria and gradient limits at the same time. Recently, *Kara et al.* [2000] introduced an optimal algorithm for ILD and MLD calculation based on δT and $\delta\sigma_\theta$ with the additional requirement that the adjacent temperature (or density) values at consecutive depths must differ less than $0.1\delta T$ and $0.1\ \delta\sigma_\theta$. The so-called split-and-merge method of MLD calculation has also been recently suggested by *Thompson and Fine* [2003].

[55] It should be noted that the use of an objective criterion to calculate the MLD may often lead to an erroneous outcome, if the set of data is significantly heterogeneous (see discussion by *Brainerd and Gregg* [1995]). A mix of profiles with sharp and weak pycnoclines underlying the MLD creates a problem of employing a unique δT or $\delta\sigma_\theta$ threshold. Therefore, if a limited data set is analyzed, it is instructive to verify the results of automatic routines by manual check-ups. In examining temperature and density NB and MSS profiles, we have used the traditional approach based on δT and equivalent $\delta\sigma_\theta$ criteria as initial guidelines, but the final identification was made by inspection. A comparison between this semi-objective approach and that of *Kara et al.* [2000] is given in Figure B1a for 30 CTD profiles having vertical resolution $dz = 2$ m. Only those profiles where MLD exceeds 6 m are used in this analysis. Our calculations of MLD have been made with initial $\delta\sigma_\theta = 0.02\ \sigma_\theta$ followed by manual correction only to four profiles. The MLD at majority of stations was almost the same as ILD.

[56] The algorithm of *Kara et al.* [2000] was applied to the same profiles by varying δT in the range 0.1°–0.3°C

with 0.05°C increment. The best consistency between the two methods was attained for δT = 0.25°C without any vertical averaging or interpolation (see Figure B1a). A strong linear regression between MLD and ILD (coefficient of determination r^2 = 0.95) indicates that automatically calculated depths of UQHL are about 5 m larger than those obtained semi-objectively, but both methods produce consistent outcomes. During further analyses, we used only the MLD estimates obtained semi-objectively, because it provides more accurate identification of the transition region between the mixed layer and thermohalocline. When both NB and MSS profiles were made in parallel, the MLD obtained from both instruments yielded almost similar values (Figure B1b). The observed scatter can in part be attributed to the mismatch of the measurement times of NB and MSS that could be as much as 1 hour.

[57] **Acknowledgments.** The CTD measurements reported herein were carried out by a group of Russian oceanographers led by V. Tereshchenkov and E. Morozov. Onboard calibration of the CTD channels and meteorological observations were made by a group of students from the Moscow State University under supervision of S. Dobrolyubov. K. Kreyman (McMaster University, Canada), F. Gomez (University of Girona), L. and E. Montenegro (both at ASU) participated in the microstructure measurements. We express gratitude to all our collaborators and to the crew of R/V Akademik Ioffe. The cruise was organized with financial support of Russian Ministry of Science and Technology. The authors received partial support from the US Office of Naval Research, grant N00014-97-1-0140 (I.L. and H.J.S.F.), and NATO 2002 Research Fellowship (I.L.); ANUIES and CICESE, Mexico (M.F.); Spanish Government, grant REN2001-2239, and Agencia Catalana de l'Aigua (E.R.); and by the Russian Foundation for Basic Research, grant 02-05-64408 (S.S.). We appreciate useful comments of two anonymous reviewers.

References

Anis, A., and J. N. Moum (1995), Surface wave-turbulence interactions: Scaling epsilon near the sea surface, *J. Phys. Oceanogr.*, *25*, 2025–2045.

Bathen, K. H. (1972), On the seasonal changes in the North Pacific Ocean, *J. Geophys. Res.*, *77*, 7138–7150.

Bolding, K., H. Burchard, T. Pohlmann, and A. Stips (2002), Turbulent mixing in the northern North Sea: A numerical model study, *Cont. Shelf Res.*, *22*(18-19), 2707–2724.

Brainerd, K. E., and M. C. Gregg (1995), Surface mixed and mixing layer depths, *Deep Sea Res.*, *42*, 1521–1544.

Burchard, H., K. Bolding, T. P. Rippeth, and A. Stips (2002), Microstructure of turbulence in the northern North Sea: A comparative study of observations and model simulations, *J. Sea Res.*, *47*(3-4), 223–238.

Bussinger, J. A., J. C. Wyngaard, Y. Issumi, and E. F. Bradley (1971), Flux profile relationships in the atmospheric surface layer, *J. Atmos. Sci.*, *28*, 181–189.

Chereskin, T. K., and D. Roemmich (1991), A comparison of measured and wind-derived Ekman transport at 11°N in the Atlantic Ocean, *J. Phys. Oceanogr.*, *21*, 869–878.

Dillon, T. M., J. G. Richman, C. G. Hansen, and M. D. Pearson (1981), Near-surface turbulence measurements in a lake, *Nature*, *290*, 390–392.

Dyer, A. J. (1974), A review of flux-profile relations, *Boundary Layer Meteorol.*, *1*, 363–372.

Ehret, L. L., and J. J. O'Brien (1989), Scales of North Atlantic wind stress curl determined from the comprehensive ocean-atmosphere data set, *J. Geophys. Res.*, *94*, 831–841.

Gregg, M. C. (1999), Estimation and geography of diapycnal mixing in the stratified ocean, in *Physical Processes in Lakes and Oceans*, *Coastal Estuarine Stud*., vol. 54, edited by J. Imberger, pp. 305–338, AGU, Washington, D. C.

Gregg, M. C., D. P. Winkel, T. B. Sanford, and H. Peters (1996), Turbulence produced by internal waves in the oceanic thermocline at mid and low latitudes, *Dyn. Atmos. Oceans*, *24*(1-4), 1–14.

Halpern, D., W. Knauss, O. Brown, M. Freilich, and F. Wentz (1994), An atlas of monthly distributions of SSM/I surface wind speed, ARGOS buoy 2 drift, AVHRR/2 sea surface temperature, AMI surface wind components, and ECMWF surface wind components during 1992, *JPL Publ.*, *94-4*, 143 pp.

Hamming, R. W. (1983), *Digital Filters*, 2nd ed., Prentice-Hall, Upper Saddle River, New Jersey.

Hellerman, S., and M. Rosenstein (1983), Normal monthly wind stress over the world ocean with error estimates, *J. Phys. Oceanogr.*, *3*, 1093–1104.

Huang, R. X., and S. Russell (1994), Ventilation of the subtropical North Pacific, *J. Phys. Oceanogr.*, *24*, 2589–2605.

Imberger, J. (1985), The diurnal mixed layer, *Limnol. Oceanogr.*, *30*, 737–770.

Imberger, J., and G. N. Ivey (1991), On the nature of turbulence in a stratified fluid: 2. Application to lakes, *J. Phys. Oceanogr.*, *21*, 659–680.

Inall, M. E., T. P. Rippeth, and T. J. Shervin (2000), Impact of nonlinear waves on the dissipation of internal tidal energy at a shelf break, *J. Geophys. Res.*, *105*(C4), 8687–8705.

Kantha, L. H., and C. A. Clayson (2000a), *Numerical Models of Oceans and Oceanic Processes*, *Int. Geophys. Ser.*, vol. 66, 750 pp., Elsevier, New York.

Kantha, L. H., and C. A. Clayson (2000b), *Small Scale Processes in Geophysical Fluid Flows*, (*Int. Geophys. Ser.*, vol. 67, 750 pp., Elsevier, New York.

Kara, A. B., P. A. Rochford, and H. E. Hurlburt (2000), An optimal definition for ocean mixed layer depth, *J. Geophys. Res.*, *105*(C7), 16,803–16,821.

Kelly, K. A., and B. Qiu (1995), Heat flux estimates for the western North Atlantic: I. Assimilation of satellite data into a mixed layer model, *J. Phys. Oceanogr.*, *25*, 2344–2360.

Kit, E., E. Strang, and H. J. S. Fernando (1997), Measurement of turbulence near shear-free density interfaces, *J. Fluid Mech.*, *334*, 293–314.

Korchashkin, N. N. (1976), Statistics of fine structure of hydrophysical fields in the ocean (in Russian), *Okeanologiya*, *14*, 602–607.

Lamb, P. J. (1984), On the mixed layer climatology of the North and tropical Atlantic, *Tellus, Ser. A*, *36*, 292–305.

Lass, H. U., H. Prandke, and B. Liljebladh (2003), Dissipation in the Baltic proper during winter stratification, *J. Geophys. Res.*, *108*(C6), 3187, doi:10.1029/2002JC001401.

Lazier, J. R. N., and D. G. Wright (1993), Annual velocity variations in the Labrador Current, *J. Phys. Oceanogr.*, *23*, 659–678.

Lentz, S. J. (1992), The surface boundary layer in coastal upwelling regions, *J. Phys. Oceanogr.*, *22*, 1517–1539.

Levitus, S. (1982), Climatological atlas of the world ocean, *NOAA Prof. Pap. 13*, 173 pp., U.S. Govt. Print. Off., Washington, D. C.

Lewis, M. R., M. Carr, G. Feldman, W. Esaias, and C. McClain (1990), Influence of penetrating solar radiation on the heat budget of the equatorial Pacific Ocean, *Nature*, *347*, 543–544.

Lombardo, C. P., and M. C. Gregg (1989), Similarity scaling of viscous and thermal dissipation in a convecting surface boundary layer, *J. Geophys. Res.*, *94*, 6273–6284.

Lozovatsky, I. D., A. L. Berestov, and A. S. Ksenofontov (1998), Phillips theory of turbulence generated fine-structure: Numerical and stochastic modeling, paper presented at Johns Hopkins Conference in Environmental Fluid Mechanics, Johns Hopkins Univ., Baltimore, Md.

Lozovatsky, I. D., T. M. Dillon, A. Y. Erofeev, and V. N. Nabatov (1999), Variations of thermohaline and turbulent structure on the shallow Black Sea shelf in the beginning of autumn cooling, *J. Mar. Syst.*, *21*, 255–282.

Lukas, R., and E. Lindstrom (1991), The mixed layer of the western equatorial Pacific, *J. Geophys. Res.*, *96*, 3343–3357.

Marshall, J., H. Johnson, and J. Goodman (2001), A study of the interaction of the North Atlantic Oscillation with ocean circulation, *J. Clim.*, *14*, 1399–1421.

Martin, P. J. (1985), Simulation of mixed layer at OWS November and Papa with several models, *J. Geophys. Res.*, *90*, 903–916.

McPhee, M. G., and T. P. Stanton (1996), Turbulence in the statically unstable oceanic boundary layer under Arctic leads, *J. Geophys. Res.*, *101*, 6409–6428.

McPhee, M. G., S. F. Ackley, P. Guest, B. A. Huber, D. G. Martinson, J. H. Morison, R. D. Muench, L. Padman, and T. P. Stanton (1996), The Antarctic Zone Flux Experiment, *Bull. Am. Meteorol. Soc.*, *77*(6), 1221–1232.

Miller, J. R. (1976), The salinity effect in a mixed layer ocean model, *J. Phys. Oceanogr.*, *6*, 29–35.

Monin, A. S., and A. M. Obukhov (1954), Basic turbulent mixing laws in the atmospheric surface layer, *Trudy Geofiz. Inst. AN SSSR*, *24*(151), 163–187.

Monterey, G., and S. Levitus (1997), *Seasonal Variability of Mixed Layer Depth for the World Ocean*, *NOAA Atlas NES-DIS 14*, 100 pp., U.S. Govt. Print. Off., Washington, D. C.

Moum, J. N., and R. G. Lueck (1985), Causes and implications of noise in oceanic dissipation measurements, *Deep Sea Res.*, *32*(4), 379–390.

Moum, J. N., D. R. Caldwell, and C. A. Paulson (1989), Mixing in the equatorial surface layer and thermocline, *J. Geophys. Res.*, *94*, 2005–2022.

Nasmyth, P. W. (1970), Oceanic turbulence, Ph.D. dissertation, Univ. of B. C., Vancouver, B. C., Canada.

Niiler, P. P., and E. B. Kraus (1977), One-dimensional models, in *Modeling and Prediction of the Upper Layers of the Ocean*, edited by E. B. Kraus, pp. 143–172, Elsevier, New York.
Oakey, N. S., and J. A. Elliot (1982), Dissipation within the surface mixed layer, *J. Phys. Oceanogr.*, *12*, 171–185.
Obata, A., J. Ishazaka, and M. Endoh (1996), Global verification of critical depth theory for phytoplankton bloom with climatological in situ temperature and satellite ocean color data, *J. Geophys. Res.*, *101*, 20,657–20,667.
Padman, L., and T. M. Dillon (1991), Turbulent mixing near the Yermak Plateau during the Coordinate Eastern Arctic Experiment, *J. Geophys. Res.*, *96*, 4769–4782.
Paka, V. T., V. N. Nabatov, I. D. Lozovatsky, and T. M. Dillon (1999), Ocean microstructure measurements by BAKLAN and GRIF, *J. Atmos. Oceanic Technol.*, *16*, 1519–1532.
Panchev, S., and D. Kesich (1969), Energy spectrum of isotropic turbulence at large wavenumbers, *C. R. Acad. Bulg. Sci.*, *22*, 627–630.
Peters, H., M. C. Gregg, and J. M. Tool (1989), Meridional variability of turbulence through the equatorial undercurrent, *J. Geophys. Res.*, *94*, 18,003–18,009.
Pollard, R. T., and J. Read (1989), A method for calibrating ship-mounted acoustic Doppler profilers and the limitations of gyro compasses, *J. Atmos. Oceanic Technol.*, *6*, 859–865.
Pollard, R. T., P. B. Rhines, and O. R. Y. Thompson (1973), The deepening of the wind-mixed layer, *Geophys. Fluid Dyn.*, *3*, 381–404.
Prandke, H., and A. Stips (1998), Test measurements with an operational microstructure-turbulence profiler: Detection limit of dissipation rates, *Aquat. Sci.*, *60*, 191–209.
Prandke, H., K. Holtsch, and A. Stips (2000), MITEC technology development: The microstructure/turbulence measuring system MSS, *Tech. Rep. EUR 19733 EN*, Eur. Comm., Joint Res. Cent., Ispra, Italy.
Price, J. E., R. A. Weller, and R. Pinkel (1986), Diurnal cycling: Observations and models on the upper ocean response to diurnal heating, cooling and wind mixing, *J. Geophys. Res.*, *91*, 8411–8427.
Qu, P. (2003), Mixed layer heat balance in the western North Pacific, *J. Geophys. Res.*, *108*(C7), 3242, doi:10.1029/2002JC001536.
Richards, K. J., M. E. Inall, and N. C. Wells (1995), The diurnal mixed layer and upper ocean heat budget in the western equatorial Pacific, *J. Geophys. Res.*, *100*, 6865–6879.
Richman, J., and C. Garrett (1977), The transfer of energy and momentum by the wind to the surface mixed layer, *J. Phys. Oceanogr.*, *7*, 876–881.
Schneider, N., and P. Muller (1990), The meridional and seasonal structures of the mixed-layer depth and its diurnal amplitude observed during the Hawaii-to-Tahiti Shuttle Experiment, *J. Phys. Oceanogr.*, *20*, 1395–1404.
Shay, T. J., and M. C. Gregg (1984), Convectively driven turbulent mixing in the upper ocean, *Nature*, *310*, 282–285.
Simpson, J. H., W. R. Crawford, T. R. Rippeth, A. R. Campbell, and J. V. S. Cheok (1996), The vertical structure of turbulent dissipation in shelf seas, *J. Phys. Oceanogr.*, *26*, 1579–1590.
Smyth, W. D., P. O. Zavialov, and J. N. Moum (1997), Decay of turbulence in the upper ocean following sudden isolation from surface forcing, *J. Phys. Oceanogr.*, *27*, 810–822.
Soloviev, A. V., N. V. Vershinsky, and V. A. Bezverchnii (1988), Small-scale turbulence measurements in the thin surface layer of the ocean, *Deep Sea Res.*, *35*, 1859–1874.
Soloviev, A., R. Lukas, and P. Hacker (2001), An approach to parameterization of the oceanic turbulent boundary layer in the western Pacific warm pool, *J. Geophys. Res.*, *106*, 4421–4435.
Spall, M. A. (1991), Diagnostic study of the wind- and buoyancy-driven North Atlantic circulation, *J. Geophys. Res.*, *96*, 18,509–18,518.
Stips, A., H. Burchard, K. Bolding, and W. Eifter (2002), Modeling of convective turbulence with a two-equation k-ε turbulence closure scheme, *Ocean Dyn.*, *52*, 153–168.
Stull, R. B. (1988), *An Introduction to Boundary Layer Meteorology*, 666 pp., Springer, New York.
Tereshchenkov, V. P., S. M. Shapovalov, S. A. Dobrolyubov, and E. G. Morozov (2002), Cruise 9 of R/V *Akademik Ioffe*, *Oceanology*, *42*(2), 298–301.
Terray, E. A., M. A. Donelan, Y. C. Agrawal, W. M. Drennan, K. K. Kahma, A. J. Williams III, P. A. Hwang, and S. A. Kitaigorodski (1996), Estimates of kinetic energy dissipation under breaking waves, *J. Phys. Oceanogr.*, *26*, 792–807.
Thompson, R. (1976), Climatological models of the surface mixed layer of the ocean, *J. Phys. Oceanogr.*, *6*, 496–503.
Thompson, R. E., and I. V. Fine (2003), Estimating mixed layer depth from oceanic profile data, *J. Atmos. Oceanic Technol.*, *20*, 319–329.
Wagner, R. G. (1996), Decadal scale trends in mechanisms controlling meridional sea surface temperature gradients in the tropical Atlantic, *J. Geophys. Res.*, *101*, 16,683–16,694.
Weatherly, G. L., and P. L. Martin (1978), Structure and dynamics of oceanic bottom boundary-layer, *J. Phys. Oceanogr.*, *8*, 557–570.
Wijffels, S. E., E. Firing, and H. L. Bryden (1994), Direct observations of the Ekman Balance at 10°N in the Pacific, *J. Phys. Oceanogr.*, *24*, 1666–1679.
Willebrand, J. (1978), Temporal and spatial scales of the wind field over the North Pacific and North Atlantic, *J. Phys. Oceanogr.*, *8*, 1080–1094.
Zilitinkevich, S. S., and I. N. Esau (2002), On integral measures of the neutral barotropic planetary boundary layer, *Boundary Layer Meteorol.*, *104*, 371–379.

H. J. S. Fernando and I. Lozovatsky, Environmental Fluid Dynamics Program, Mechanical and Aerospace Engineering, Arizona State University, Tempe, AZ 85287-9809, USA. (i.lozovatsky@asu.edu)

M. Figueroa, Department of Physical Oceanography, Centro de Investigación Científica y Educación Superior de Ensenada, Ensenada, Baja California, Mexico.

E. Roget, University of Girona, Campus de Montilivi, E-17071 Girona, Spain.

S. Shapovalov, P. P. Shirshov Institute of Oceanology, Russian Academy of Sciences, Moscow, Russia.